SEARS
Ship Emissions to Atmosphere
Reporting Service
Contract No. 400104295

D4 - Potential of future instruments to detect NO_2 from ships over European waters

Reference: SEARS_D4_Future_Instruments
Issue 2.0
Date: October 2014
Prepared for: ESA

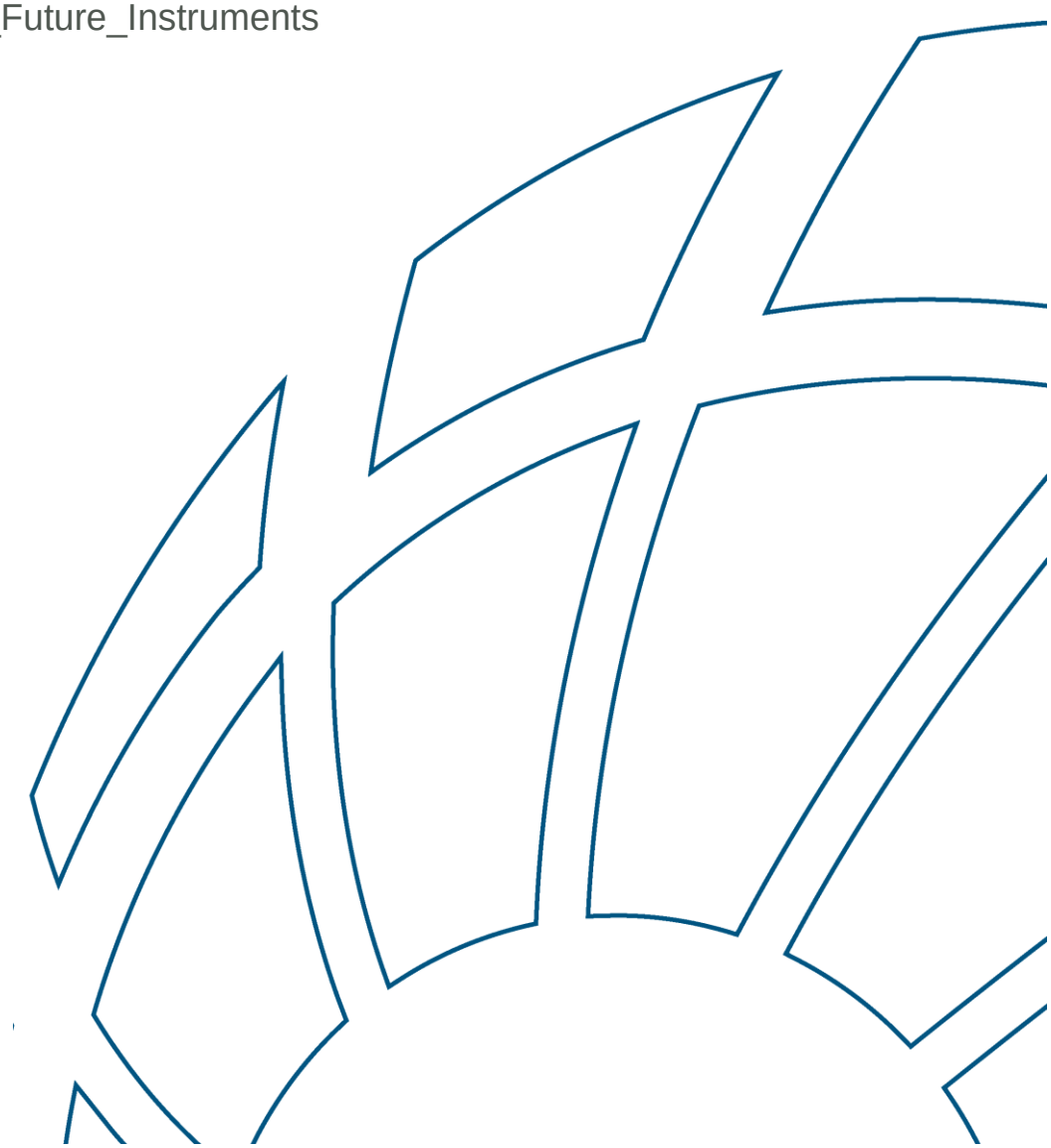

Document status sheet

Title	: D4 – Technical report on the potential of future instruments to detect NO_2 from ships over European water
Code	: SEARS-D4
Date	: October 2014
Status	: Final
Issue	: 2.0
Contractnr	: 4000104295/11/I-NB
Projectnr	: A11025
Project name	: SEARS
Prepared for	: ESA
Author(s)	: Huan Yu (BIRA) Michel van Roozendael (BIRA) Isabelle de Smedt (BIRA) Andreas Richter (IUP-UB) Andreas Hilboll (IUP-UB) Gerard Hesselmans (HERMESS) Agnes Mika (BMT ARGOSS)
Approved by	: Hein Zelle (BMT ARGOSS)
Distribution	: ESA EMSA BMT ARGOSS IUP BIRA HERMESS

Contents

LIST OF ABBREVIATIONS AND ACRONYMS **1**

1. INTRODUCTION **1**

2. MODELLING AND SATELLITE SENSORS **2**

2.1. MODELLING SET-UP 2
2.2. TROPOMI ON BOARD OF SENTINEL-5 PRECURSOR 2
2.3. SENTINEL-4 2

3. PREPARATION OF PSEUDO-OBSERVATIONS OF NO_2 DATA SET **4**

3.1. EVALUATION OF CTM AND OMI TROPOSPHERIC NO_2 COLUMNS 4
3.2. SENTINEL-5 5
3.2.1. Geometry *5*
3.2.2. Estimation of the error on NO_2 SCDs *6*
3.2.3. Cloud representation *8*
3.2.4. Meteorology *11*
3.3. SENTINEL-4 11
3.3.1. Geometry *11*
3.3.2. Air mass factors *13*
3.3.3. Estimation of Error on NO2 SCs *14*
3.3.4. Cloud representation *14*

4. SENSITIVITY STUDY FOR FUTURE SENSORS **16**

4.1. SENTINEL-5 16
4.1.1. Impact of the spatial resolution *16*
4.1.2. Improvement of the error on NO_2 SCDs *17*
4.1.3. Cloud effect *20*
4.1.4. Wind effect *21*
4.1.5. Sun glint effect *22*
4.2. SENTINEL-4 22
4.2.1. Detectability of monthly shipping NO_2 signals *23*
4.2.2. Detectability of daily shipping NO_2 signals *27*

5. SUMMARY **30**

5.1. SENTINEL-5 30
5.2. SENTINEL-4 30

6. REFERENCES **32**

APPENDIX A METEOROLOGICAL AND CHEMISTRY-TRANSPORT MODELLING **33**

A.1 METEOROLOGICAL MODELLING 33
A.1.1 The WRF model *33*
A.1.2 Model setup *34*
A.1.3 MODELLING STRATEGY AND OUTPUT DATA 38
A.2 AIR QUALITY MODELLING 38
A.2.1 CHIMERE chemistry-transport model *38*
A.2.2 CHIMERE pre-processor *39*
A.2.3 Emission databases *40*

A.2.4 Correspondence between IPCC (EDGAR) and SNAP (EMEP) activity sectors *42*

A REFERENCES **44**

List of abbreviations and acronyms

BB	Bay of Biscay
BIRA	Belgian Institute for Space Aeronomy
CF	Cloud Fraction
COT	Cloud Optical Thickness
CP	Cloud Pressure
CTM	Chemistry-Transport Model
ECMWF	European Centres for Medium-range Weather Forecasts
EMS	East Mediterranean Sea
FOV	Field of View
GMES	Global Monitoring of the Environment and Security
GOME-2	Global Ozone Monitoring Experiment-2
IUP	Institute of Environmental Physics (University of Bremen)
LT	Local Time
MODIS	Moderate Resolution Imaging Spectroradiometer
NS	North Sea
OMI	Ozone Monitoring Instrument
OZA	Observation Zenith Angle
OAA	Observation Azimuth Angle
RAA	Relative Azimuth Angle
S4	Sentinel-4
S5P	Sentinel-5 Precursor
SAA	Solar Azimuth Angle
SCD	Slant Column Density
SCIAMACHY	Scanning Imaging Absorption spectrometer for Atmospheric CartograpHY
SNR	Signal-to-noise ratio
STD	STandard Deviation
SZA	Solar Zenith Angle
TEMIS	Tropospheric Emission Internet Service
TROPOMI	TROPOspheric Monitoring Instrument
VCD	Vertical Column Density
UV	UltraViolet
NIR	Near-infrared
SWIR	Shortwave infrared

1. Introduction

In recent years, space-borne spectrometers, such as GOME, SCIAMACHY, OMI, and GOME-2, have been used to detect and quantify NO_2 pollution sources due to shipping emissions. Although these satellite instruments are limited in their ability to provide useful data with a time resolution better than typically one month or longer, they have provided useful information on the seasonal and inter-annual variability in shipping emissions as well as on their long term trends.

Current shipping NO_2 products are limited by four main factors: signal to noise ratio, spatial and temporal resolution, cloud and/or aerosol contamination, and difficulty to separate shipping NO_2 from other sources of emissions. Improvements on the first three of these points can be expected from future satellite instruments, in particular the Sentinel-5 precursor (S5P) and the Sentinel-4 (S4) that are planned to be launched during the current decade. Both instruments will have better spatial resolution, comparable or better coverage and better signal-to-noise ratios than current sensors. Better spatial resolution reduces cloud contamination and increases signal for localized sources such as ships. Improved coverage (which will be available over Europe with S4 flying on the geostationary orbit) improves statistics for cloud free pixels and thereby reduces noise. This can even be further improved by combining data from several instruments operating at the same time, e.g., combining data from GOME-2, OMI, and other instruments. Based on these considerations, it is anticipated that future sensors will allow for significant improvement of the time resolution of the shipping NO_2 products therefore matching better the requirements from International Maritime Organizations such as EMSA.

The purpose of this technical report is to investigate more quantitatively the gain to be expected from future sensors. Our focus is on three areas over European waters: The East Mediterranean Sea (EMS), the Bay of Biscay (BB), and the North Sea (NS). These are relatively polluted regions with significant contributions from dense ship traffic. A regional chemical transport model (CHIMERE) combined with a high-resolution emission inventory is used to generate NO_2 profile data with high spatial ($10\times10 km^2$) and temporal (hourly) resolution. These NO_2 data sets are used to generate pseudo-observations for the future sensors, as well as for OMI as a reference. The pseudo-observation satellite data sets are compared to the existing data records of OMI, and used to assess the potential of future sensors for identifying shipping emissions.

The document is set up as follows:

- Section 2 introduces the CTM and describes the future S5P and S4 sensors.
- Section 3 builds instrument models for the future sensors.
- Section 4 assesses what will be the expected improvement from TROPOMI and Sentinel-4 relative to existing sensors.
- Section 5 summarizes the capabilities of the future instruments for shipping NO_2 retrieval.

2. Modelling and satellite sensors

2.1. Modelling set-up

The modelling set-up consists of a nested version of the CHIMERE chemistry and transport model coupled to WRF meteorology. Details of the model set-up including emission inventories and domain are given in Appendix A.

2.2. TROPOMI on board of Sentinel-5 Precursor

To be launched in early 2016, the S5P mission flies on a low Earth orbit polar satellite system to provide information and services on air quality, climate, and the ozone layer in the timeframe 2016-2022. The S5P mission is part of the Global Monitoring of the Environment and Security (GMES) or now COPERNICUS space component programme. It consists of a satellite bus, the TROPOspheric Monitoring Instrument (TROPOMI), and a ground segment. A comprehensive description of the mission can be found in Veefkind et al. (2012).

The S5P reference orbit is a near-polar frozen sun-synchronous orbit adopted for optimization of the mission with a mean local solar time at ascending node of 13:30h and a repeat cycle of 17 days. The orbital height is nominally 824km and has been selected to fly in formation with the U.S. NPP mission.

The only payload of the S5P mission is the TROPOMI instrument, which is jointly developed by The Netherlands and ESA. TROPOMI is a two-dimensional grating spectrometer with spectral bands in the UV, the visible, the NIR, and the SWIR. The selected wavelength range for TROPOMI allows observation of key atmospheric constituents, including O_3, NO_2, SO_2, CO, CH_4, HCHO, aerosols, and clouds. S5P provides daily global coverage, a spatial resolution of $7\times7km^2$, and an improved signal-to-noise in comparison to the heritage OMI instrument (Levelt et al., 2006). S5P will be the first GMES atmospheric sentinel filling the gap in high-resolution tropospheric pollutant monitoring until the launch of the Sentinel-5 mission that is planned for 2020 onwards. It will also continue the historical long-term UV-Vis data record of GOME, SCIAMACHY, and OMI as well as the SWIR measurements of SCIAMACHY. In addition, the early afternoon observations of TROPOMI will provide a strong synergy with the morning observations of GOME-2 on MetOp A, B, and C.

2.3. Sentinel-4

The Sentinel-4 mission will consist of an UVN (Ultraviolet-Visible-Near-Infrared) spectrometer accommodated on Meteosat Third Generation Sounder (MTG-S) platforms operating in geostationary orbits. Two missions are planned for the S-4 UVN payload: the first one in 2019 and the follow-up mission in 2027.

The mission objective of the Sentinel-4 is the continuous monitoring of atmospheric composition and air quality in Europe (O_3, NO_2, SO_2, HCHO, and aerosol optical depth) at a fast revisit time of ~1 hour. The spectral resolution of the UVN instrument will be 0.5 nm in the UV/visible and 0.12 in the NIR. Spatial sampling will be 8 km at 45°N.

With its geostationary orbit, Sentinel-4 UVN will for the first time provide hourly observations over Europe, increasing measurement statistics, reducing sensitivity to clouds, and enabling

studies of the diurnal variation of emissions, chemistry, and transport of pollutants. As the spatial coverage of UVN is limited to Europe, it will be operated in combination with low earth orbiting instruments such as S5P and S5.

3. Preparation of pseudo-observations of NO_2 data set

3.1. Evaluation of CTM and OMI tropospheric NO_2 columns

We compared CHIMERE CTM simulations of tropospheric NO_2 columns for 12:00UT with the observed OMI columns for 2007 (Figure 3.1). Spatial patterns revealed by OMI and CHIMERE for these annual averages show good agreement, but the simulated columns are lower than OMI observations over urban and industrial areas. If in an attempt to improve the OMI data sets, high-resolution CHIMERE profiles are used to calculate NO_2 AMFs instead of the coarse resolution TM4 model (used by default for TEMIS), one can see (Figure 3.1b) that the resulting tropospheric VCDs are even further enhanced over polluted regions, so that the difference between CHIMERE and the improved OMI NO_2 dataset reaches a factor of 1.5~2.5. However, if the CHIMERE NO_2 columns are doubled to restore a good agreement with observations over urban areas (Figure 3.1d), the modelled NO_2 VCDs will be higher than satellite measurements over background regions.

In order to evaluate the CHIMERE and OMI tropospheric NO_2 columns over the ship lanes, a linear background fit approach (Vinken et al., 2013) is used to extract the NO_2 signal from shipping emissions. Data is averaged along the ship track to get better signal-to-noise ratio (see Figure 3.2). The figure shows that using this approach OMI and the doubled/tripled model data display high consistency of the shipping NO_2 signal over EMS and BB respectively, and only a small shift (0.05°/0.25°) in the position of the ship lane is observed. Therefore in this exploratory study, **the NO_2 data simulated by CHIMERE will be doubled/tripled over EMS/BB** to improve the consistency with satellite measurements.

Over the EMS area, the seasonal variation of the NO_2 shipping signal (Figure 3.2 top panel) inferred by both OMI and CHIMERE is very small. However, there are some differences between the satellite and the modelled NO_2 columns. NO_2 VCDs from satellite measurements show a different shape across the ship track, the peak being higher and narrower in summer than in other seasons. The variation of the width of the NO_2 peak (0.6° in winter, versus 0.35° in summer) is linked to the lifetime of NO_x and/or to a dilution effect induced by the wind. On the other hand, the seasonal changes simulated by CHIMERE are very small, and the width of the NO_2 peaks across the ship track is slightly larger than the observed one. It must be noted that the width of the measured NO_2 signal over the ship track is of the order of 30 km, meaning that the 10 × 10 km^2 resolution of the CHIMERE model appears to be appropriate for these comparisons.

For the BB region, the shipping signal can be detected from monthly OMI NO_2 maps in April, July and October, but not for January (Figure 3.2 bottom). Both OMI and CHIMERE data show a strong and consistent seasonal variation in shipping NO_2 signal, but this result is not consistent with the multiannual average NO_2 map as shown in WP2000. This difference may be linked to the inter-annual variability of meteorological data over this area. The extension of shipping NO_2 signal across the ship lane over BB (1°~1.5° of FHWM) is wider than over EMS, corresponding to a relatively wide shipping track.

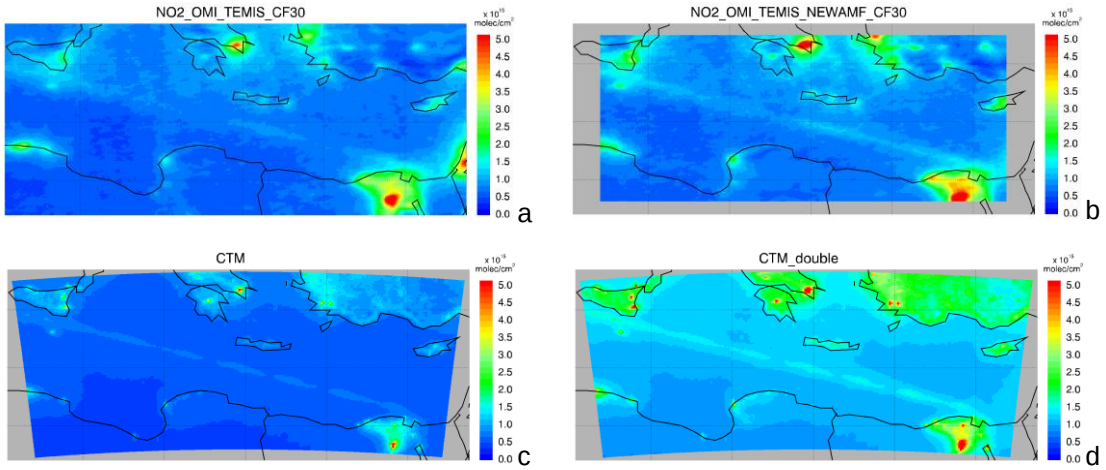

Figure 3.1: Tropospheric NO_2 VCDs over the EMS region for OMI and CHIMERE CTM for July-August 2007. a) OMI retrieval; b) improved OMI retrieval with CHIMERE profiles; only pixels with OMI cloud fraction less than 30% are used in analysis. c) CHIMERE; d) double CHIMERE NO_2.

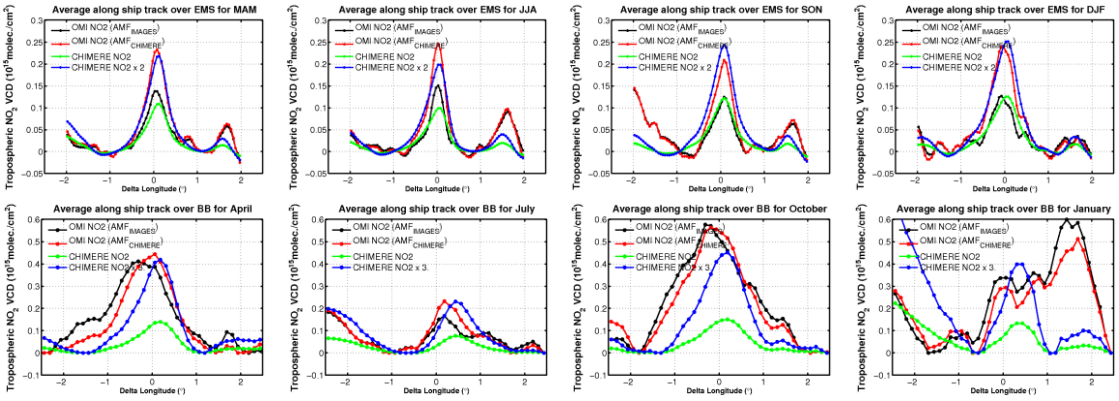

Figure 3.2: Seasonal variation of the along ship track averages of tropospheric NO_2 columns over the EMS (top) and BB (bottom) regions. Data have been spatially high-pass filtered, and a linear background fit was subtracted from the averages. See text for details.

3.2. Sentinel-5

3.2.1. Geometry

The measurement principle of TROPOMI is similar to that of OMI. The instrument images a strip of the Earth on a two dimensional detector for a period of 1 second (2 seconds for OMI) during which the observed swath moves by about 7km along its orbit. The field of view of the imaging system is large (~114°) and approximately corresponds to a swath width of 2600km. The ground pixel size at nadir position is about 7×7km^2 (along × across track) for TROPOMI. In fixed binning mode (such as OMI), the pixel size in the swath-direction increases with the viewing angle, and the across-track size at the most outer swath-angle (57°) is approximately 5 times larger than the pixel size at the nadir viewing angle. In contrast, TROPOMI adopts a variable binning factor (van Geffen et al., 2013); the binning factor is reduced by a factor of 2 and 4 at the point in the swath where the ground pixel size has doubled and quadrupled in comparison to the nadir pixel size.

Figure 3.3 shows an illustration of the typical along-swath geometries for GOME-2 (forward scan only), OMI, and simulated TROPOMI pixels derived from OMI observation. The ground pixel size at nadir position is about 7 × 7 km² for TROPOMI and 13 × 24 km² for OMI. Hence,

the OMI pixels at nadir position (rows 9-50, 0-based) were split into 2 × 3 (along × across track) parts to represent TROPOMI pixels. Likewise, the OMI pixels were split into 2 × 6 and 2 × 12 parts when the viewing zenith angle of the ground pixel is larger than 45° (rows 3–8 and 51–56) and 60° (rows 0–2 and 57–59), respectively. The satellite geometry (OZA and OAA) representative for TROPOMI observations were linearly interpolated from the corresponding OMI geometries, and solar geometry (SZA and SAA) is calculated based on the observation time and geographic location of satellite pixels.

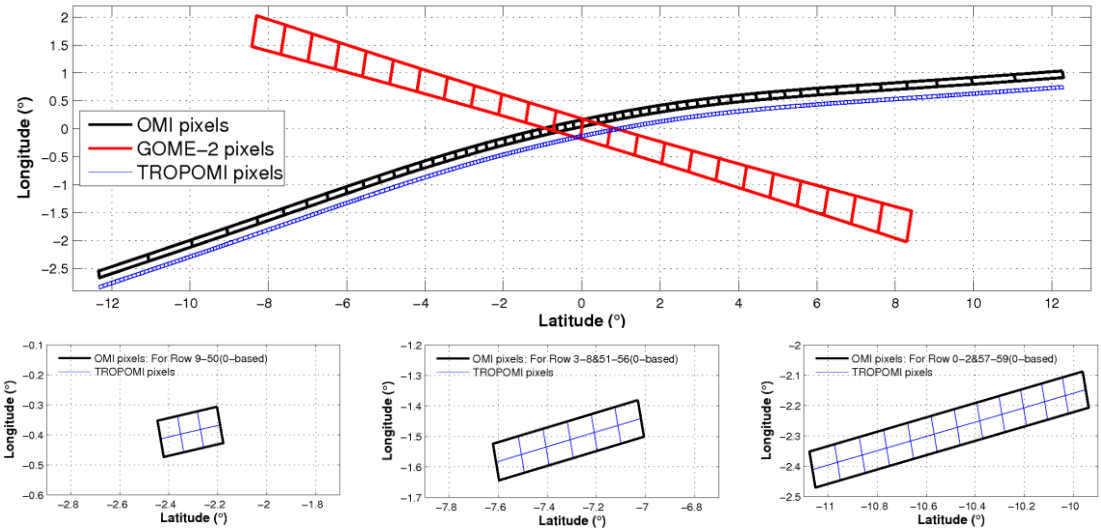

Figure 3.3: Upper panel: Comparison of OMI, GOME-2, and TROPOMI pixels; Lower panel: simulated TROPOMI pixels derived from OMI observations, left, middle and right panels represent the situations at different viewing angles. The OMI pixels were split into 2 × 3 for TROPOMI pixels at nadir position (left, row 9–50), into 2 × 6 when the size of OMI pixel is doubled (middle, row 3–8, 51–56) and into 2x12 parts when the size of OMI pixel is quadrupled (right, row 0–2, 57–59). Note that although, in reality, the along track size of the OMI pixels also increases significantly towards the swath edges (even more so than GOME-2 as the swath is larger) OMI ground pixel corner coordinates used here are based on the simplified non-overlapping (tiled) pixels product.

3.2.2. Estimation of the error on NO_2 SCDs

The precision of the NO_2 slant columns is derived from a statistical analysis of the satellite observations in the clear tropical Pacific region (5°S – 5°N; 150°E – 150°W). Since the stratospheric NO_2 columns are relatively constant over one month and the tropospheric NO_2 burden is very small in this area, spatial variations in small boxes (2° lat ×4° lon) can be neglected. Hence, the random noise of the NO_2 columns from satellite observations can be determined from the variation of the NO_2 columns within each box, as shown in Figure 3.4 for data from March 2007. In this analysis, a geometric AMF is applied to correct for the small changes in solar zenith angle and the effect of the variable line of sight angle of the observations, and only nadir measurements (VZA<40°) are used to further reduce the error from the variability of the AMF, GOME-2 backward scans are excluded in the analysis as well, and a destriping approach has been implemented in OMI SCDs to correct its spurious across-track variability (Dobber et al., 2008; Boersma et al., 2011). The figure includes the results of all GOME-2 and OMI retrievals used in this study. As can be seen, the distribution of the TEMIS NO_2 column deviations has a nearly Gaussian shape with a FWHM of 0.52×10^{15} molec cm^{-2}, which roughly corresponds to a slant column error of about 0.5×10^{15} molec cm^{-2} (≈0.42×FWHM×2.3 (average geometric AMF)). As expected, the improved GOME-2 NO_2 retrieval from IUP shows a smaller scatter (FWHM=0.43×10^{15} molec cm^{-2}). The mean OMI NO_2 slant column error (0.66×10^{15} molec cm^{-2}) is consistent with previous studies (Boersma et al., 2007) and larger than the GOME-2 error due to the smaller ground pixel size of the OMI

measurements (13×24km^2 versus 40×80km^2 for GOME-2). The slant column error also depends on the cloud fraction and surface albedo, since the instrument noise is mainly a result of the photoelectron shot noise. Figure 3.4 also shows the results of an analysis for cloud free (CF<30%) and cloudy (CF>30%) scenes. For cloud-free pixels, the error is close to the average value, but it is 15% smaller for cloudy pixels. Note that the impact of the instrumental degradation can be neglected for OMI (slant column error is about 0.65×10^{15} molec cm^{-2} for the same analysis for March 2005).

The anticipated radiometric signal-to-noise ratio (SNR) of TROPOMI in the NO_2 band (400-500nm) is 800-1000 for an individual Level-1b spectrum (van Geffen, et al., 2013), which is very similar to OMI. Hence, based on current knowledge of the instrument, the error on TROPOMI NO_2 slant columns is estimated to be of the order of 0.7×10^{15}. If further improvements are considered, such as a widening of the fitting window as for GOME-2 retrievals, the error is reduced by more than 20% (c.f. Figure 3.4). More accurate wavelength calibration and consideration of liquid water and O_2-O_2 contributions in the spectral fit will reduce the error by another 20% in the slant column retrieval (van Geffen et al., 2013), and thus ideally, the error of the NO_2 slant columns can be reduced by 50%. Note that the error of TROPOMI retrievals will increase by a factor $\sqrt{2}$ and 2 for those measurements where the binning factor is reduced by a factor of 2 and 4, respectively.

In addition, the SNR varies with the geometry of the satellite and the solar position. Figure 3.5 shows the variation of the reflected radiation at TOA (compared to the radiation in the equatorial Pacific region discussed above) for several scenarios, which represent different location, position within the satellite swath, and season at satellite (TROPOMI) overpass time. The seasonal variation is up to a factor of 2, and the differences are less than 40% between different satellite viewing angles.

In this study, the error of NO_2 SCDs at nadir is assumed to be 0.7×10^{15} molec cm^{-2} (default value for TROPOMI), 0.35×10^{15} molec cm^{-2} (best estimation for TROPOMI), 1.7×10^{15} molec cm^{-2} (equivalent OMI error and worst case for TROPOMI), and these values are increased according to changes in the binning factor following the principle of TROPOMI measurements. Furthermore, a test case simulation for OMI with a fixed error of 0.7×10^{15} molec cm^{-2} for individual pixels is also shown in the next section.

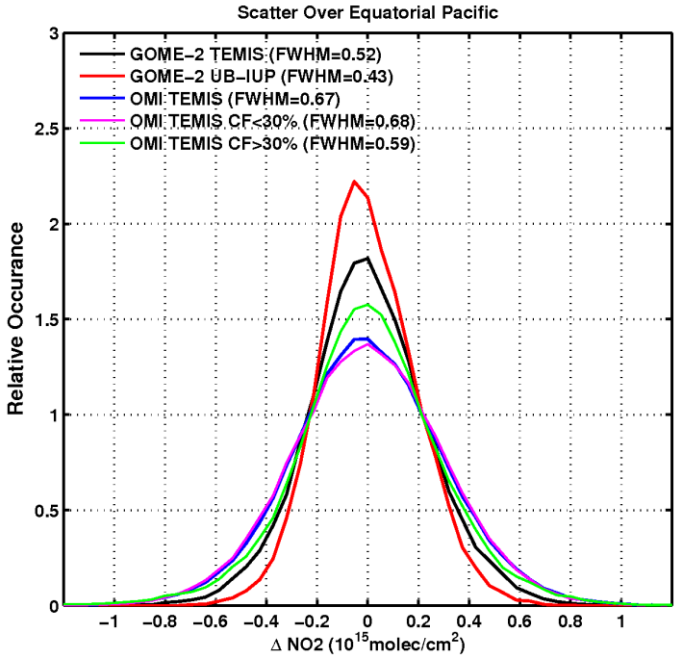

Figure 3.4: Distribution of the deviations of vertical NO_2 columns from corresponding box (2°×4° lat×lon) mean values over the tropical Pacific area (5°S-5°N, 150°E-150°W) for March 2007. A geometric AMF is applied to convert slant columns into vertical columns. Only nadir measurements (VZA<40°) are taken in account. For further details, see text.

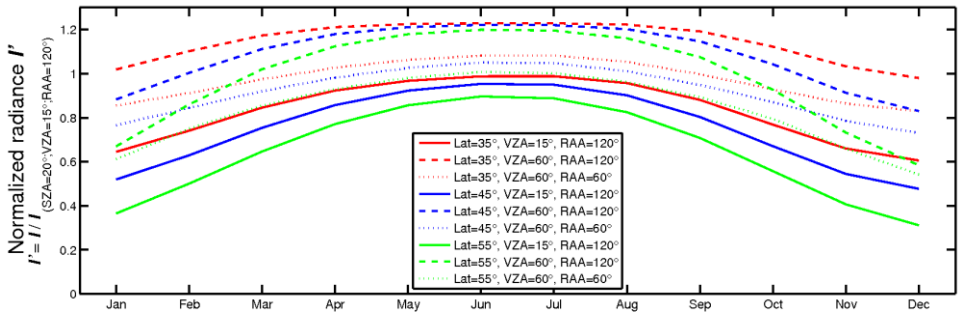

Figure 3.5: Variation of the reflected radiance at TOA, divided by the radiance measured in Tropical regions (SZA=20°, VZA=15°, RAA=120°). The three colours correspond to different locations at different latitudes (red=35°-Mediterranean Sea, blue=45°-Bay of Biscay, green=55°-North Sea), and three line types represent three positions within the TROPOMI swath (solid = nadir; dashed = right-most position; dotted = left-most position)

3.2.3. Cloud representation

A simplified Lambertian cloud model is often used for cloud correction of trace gas retrievals from UV-visible satellite spectrometers, such as GOME, SCIAMACHY, OMI, and GOME-2. In this cloud model, each pixel is assumed to consist of a clear and a cloudy part following the independent pixel approximation (or IPA). The surface is treated as a Lambertian reflector, and similarly clouds are assumed to be optically thick Lambertian reflectors (with a fixed albedo of 0.8). This means that no light is transmitted through the cloud. The fraction of the Lambertian cloud covering a pixel is called the effective cloud fraction. This fraction is not the geometric cloud fraction of the true cloud but a radiometrically equivalent cloud fraction, which in combination with the assumed cloud albedo yields a TOA reflectance that agrees with the observed reflectance. The missing transmission of this model cloud is compensated by the

large cloud-free part of the pixel. The cloud pressure is adjusted according to the depth of a spectroscopic feature such as the near-infrared O_2-A band or the visible O_2-O_2 band.

In order to match the high spatial resolution of the TROPOMI simulations, cloud products from Aura/MODIS are used in this study. These display a resolution of 1×1km² for cloud optical depth (COT) values, and 5×5km² for the cloud fraction (CF) and the cloud pressure (CP). Figure 3.6 illustrates cloud retrievals obtained from OMI O_2-O_2 and MODIS on 3rd January 2007 over the east Mediterranean Sea. Since the overpass times of MODIS and OMI are within ~15min, the spatial distribution of the cloud cover is expected to be similar. Results nevertheless indicate a poor correlation between OMI effective CF and MODIS geometric CF, which is due to the different definitions used for the CF derived from these two sensors. On the other hand, the MODIS COT shows a non-linear correlation with the OMI effective CF as demonstrated in Figure 3.7. By analogy with the approach presented in Stammes et al. (2008), we correlate MODIS COT and OMI effective CF simplified as the following equation:

$$y = 1 - e^{-x/a} \quad (1)$$

Here y is the MODIS COT and x is the OMI effective CF. a is an empirical variable adjusted to the satellite cloud datasets. Here, all pixels with OMI CF above than 99% or MODIS COT larger than 99 are excluded from the analysis. Over the east Mediterranean region, a varies from 9 to 16 depending on season, the average value being about 13 for the whole year. The variation of a affects the effective CF for scenes having small cloud fraction, but its influence is negligible for pixels with effective CF larger than 30%. Hence, no impact is expected on the selection of cloud free pixels. In addition, the calculated MODIS effective CF agrees very well with MODIS CF for cloudy pixels (CF>30%), while there is a relatively large discrepancy for less cloudy pixels. Since MODIS retrievals infer more cloud free (CF=0) pixels, it is likely to be an anomaly of the MODIS cloud retrieval. On the other hand, it seems that the COT retrieval is poorly sensitive to thin clouds, since there are a lot of pixels with a large CF (>80%) and COT=0 over this region (see Figure 3.6 c and e). In any case, this is of minor importance on our application as regards the discrimination of cloudy pixels from satellite measurements.

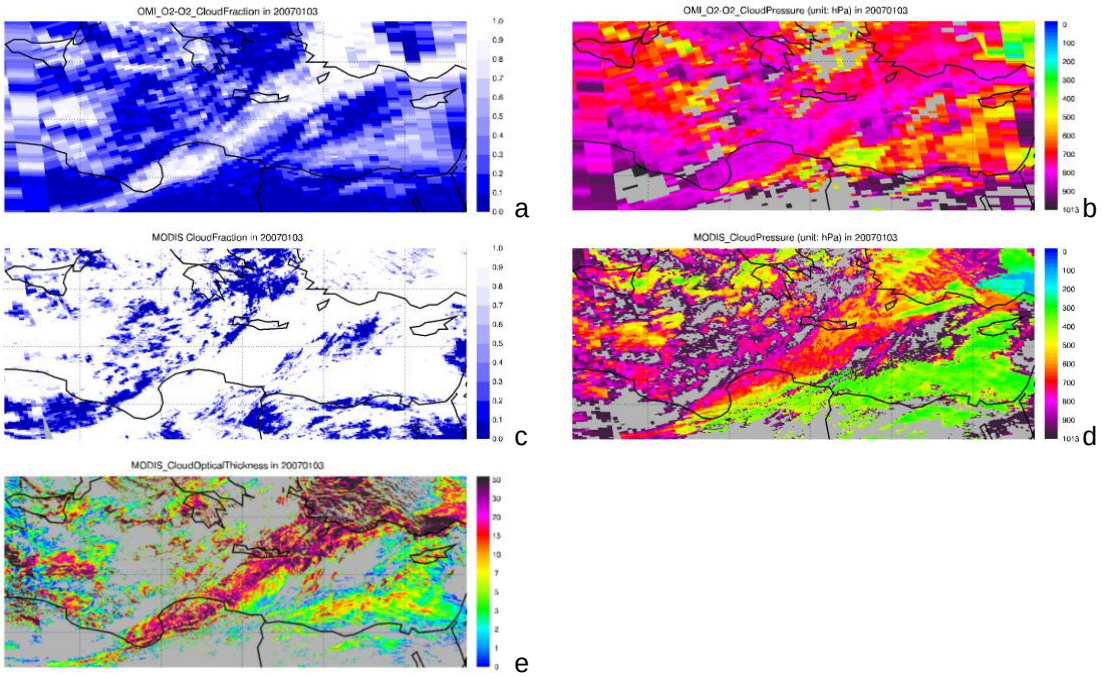

Figure 3.6: Example of cloud properties derived from satellite observations over the East Mediterranean Sea on 3rd January, 2007. a) OMI O_2-O_2(475nm) effective CF; b) OMI O_2-O_2 CP; c) MODIS (Aqua) CF; d)MODIS CP; e) MODIS CP.

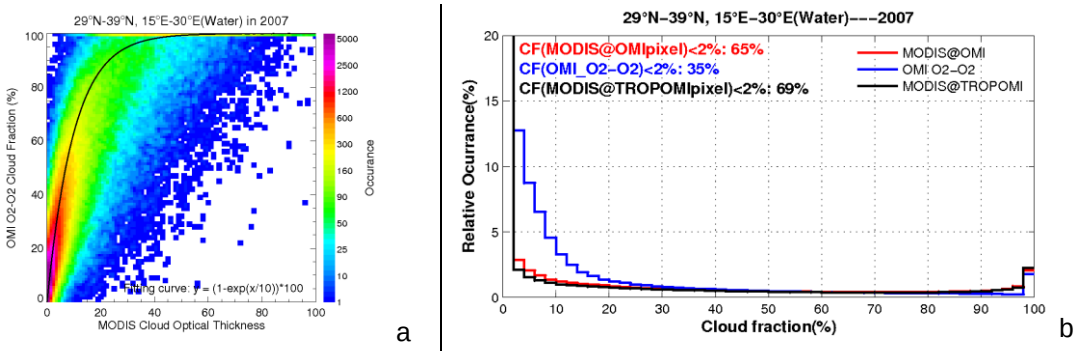

Figure 3.7: a) Scatter plot of MODIS COT versus OMI O_2-O_2 effective CF, and the corresponding fitting curve. Statistics are based on a whole year (2007) of OMI observations over the East Mediterranean. Only pixels over ocean with VZA<45° are used, and all pixels with the saturated cloud fractions (>99%) or cloud optical thickness (>99) are excluded from the analysis. b) Distribution of effective cloud fraction from different cloud algorithm, MODIS effective CF is derived from COT, based on the equation: CF=1-exp(COT/10).

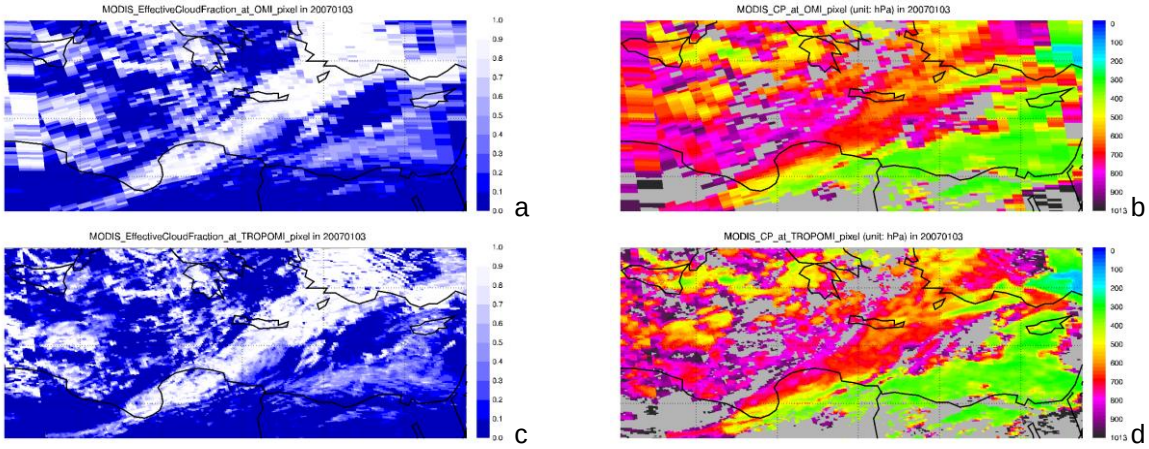

Figure 3.8: Example of effective CF and CP for OMI and TROPOMI pixels, derived from MODIS. a) Effective CF and b) CP at OMI resolution; c) Effective CF and d) CP at TROPOMI resolution.

3.2.4. Meteorology

The meteorological fields are derived from ECMWF ERA-Interim reanalysis data with a spatial resolution of 1°×1° and a frequency of 4 times a day (every 6 hours). The distribution of wind fields over Europe has been shown in WP2000; there are prevailing winds blowing from west to east at high latitudes, while at low latitudes, they show a prominent seasonal variation.

3.3. Sentinel-4

The overall approach taken for Sentinel-4 is the same as for Sentine-5. However, the differences in instrument and observation geometry necessitate some changes as outlined in the next sections.

3.3.1. Geometry

The viewing geometry of S4 differs from that of existing low Earth orbiting instruments as result of the geostationary position of the satellite. The instrument is imaging as OMI and TROPOMI, but in addition is also scanning. In the current configuration, the instrument images in the North-South direction and scans in East-West direction.

Due to instrumental and data rate limitations, the field of view of the S4 instrument is more or less limited to Europe. Not all details of the instrument and the operation are decided at this point in time, and some reasonable assumptions have been made for the simulation of the observations. These assumptions are summarized in Table 3.1.

Table 3.1: Parameters used for the simulation of S4 synthetic data

Parameter	Value
Satellite altitude	36000 km
Satellite Position	0°N, 0°E
FOV (North / South)	3.85°
FOV (East / West)	11.2°
angle increment N / S	130 microrad
angle increment E / W	210 microrad
Spatial sampling	8 km at 45°N
Repeat cycle	1 hour

As result of the observation geometry from geostationary orbit, the local observation zenith angle (OZA) of S4 changes with latitude and reaches relatively large values at high latitudes. As large OZAs limit the sensitivity of the measurements towards absorptions in the boundary layer, a threshold of 75° OZA was assumed here. This choice can be regarded as rather optimistic; in current satellite data, the limit is often set to 60° OZA to avoid reduction of sensitivity. However, as shown in Figure 3.9, this threshold would exclude all of Scandinavia, Eastern Europe, and even parts of the UK and northern Germany and is therefore not applied here.

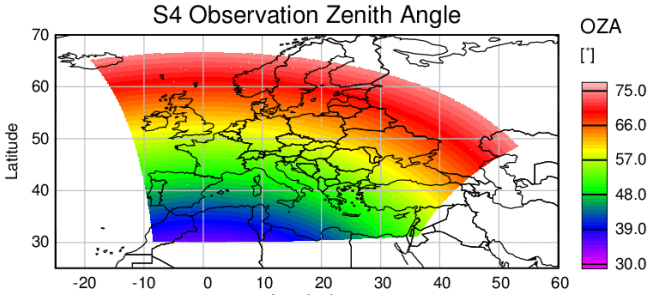

Figure 3.9: S4 Observation zenith angle

As the OZA increases, so does the size of the ground pixels for reasons of viewing geometry. While the size of the ground-pixels is simulated properly here, the effect on the NO_2 field is not considered as the resolution of the available model data is of the same order as that of the S4 pixels. The simulated measurements are therefore based on NO_2 at model resolution, and for each satellite pixel the NO_2 value from the closest model grid cell is used.

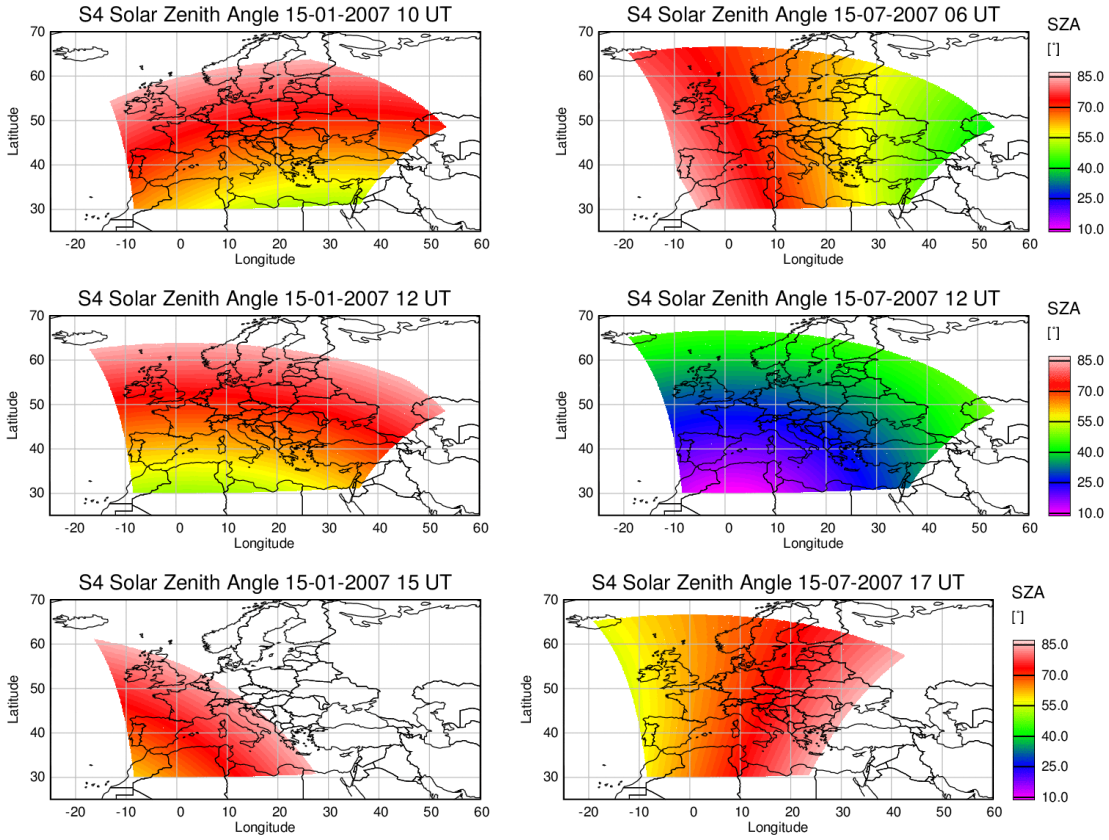

Figure 3.10: Variation of solar zenith angle over the time for January 15 (left) and July 15 (right) Note the difference in times shown for the two seasons. Only data up to 85° SZA are shown.

The main advantage of the geostationary orbit is the ability to take several measurements per day. In the case of S4, measurements are taken hourly. In practice, these observations are not instantaneous as the longitudinal scan takes time; for the sake of simplicity, the hourly NO_2 model fields are used here as if the satellite produced snapshots. As the solar position varies over the day, and at large SZA sensitivity to the lower atmosphere is lost, a SZA limit of 85° is applied. As a result, the number of S4 measurements per day varies in space and time. In Figure 3.11, the results are shown for two days in January and July. As can be seen, the number of measurements per day varies between regions and seasons, with 6 in winter (15 in summer) in the North-Sea, 8 (14) in the Bay of Biscay and 9 (13) in the Eastern Mediterranean.

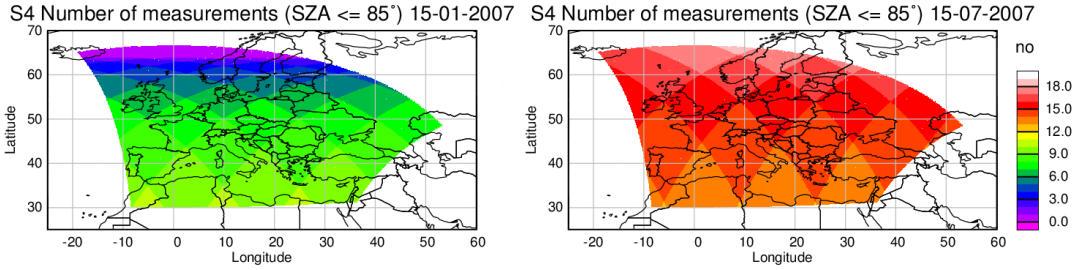

Figure 3.11: Number of S4 measurements per day having an observation zenith angle smaller than 75° and a solar zenith angle smaller than 85°. The change of solar zenith angle during the S4 scan is not taken into account. The usable number of observations is smaller due to clouds (see section 3.3.4)

3.3.2. Air mass factors

The geometry of observation by a geostationary instrument is very different from that of a low earth orbit instrument. As the instrument is at a long distance from earth, only very small changes in viewing angles are needed to scan the surface. At the same time, the solar and viewing angles at satellite differ strongly from those on the ground. Therefore, existing lookup-tables for air mass factors cannot be used.

As result of the large number of pixels of a single hourly S4 scene, radiative transfer calculations for each single pixel are time consuming and can only be performed for a limited data set. Therefore it was decided to compute altitude dependent box-AMFs for all time steps only for day 15 of each of the 4 months for which hourly model data is available (January, April, July, October). These box-AMFs are then used for all days of the month. With this approximation, the changes in solar geometry during a month are neglected, but not the changes in NO_2 vertical distribution resulting from transport and photochemistry. In the context of this sensitivity study, the uncertainties introduced by this approach were judged to be acceptable.

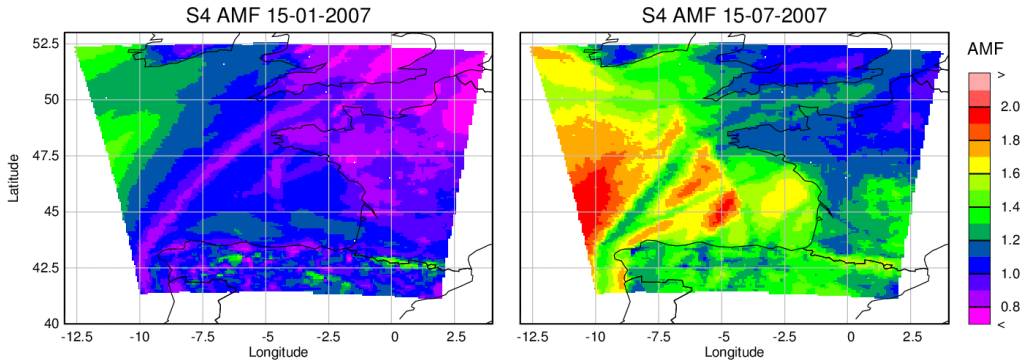

Figure 3.12: Air mass factors for NO_2 in the Gulf of Biscay area for January 15, 2007 (left) and July 15, 2007 (right), both for 12 UT.

As this study is focusing on ship emissions, a constant surface albedo of 5% is assumed. No aerosol or cloud effects are considered.

In Figure 3.12, examples are shown for the resulting air mass factors for January and July in the Gulf of Biscay region. The difference between the two months is mainly due to the difference in solar zenith angle but seasonal changes in NO_2 vertical distribution also contribute. As expected, the main shipping lanes are visible in the air mass factors as regions with low values, as there the NO_2 is close to the surface where sensitivity is smallest. This is important for the detection of ship tracks as it reduces the contrast of the retrieved slant columns.

3.3.3. Estimation of Error on NO2 SCs

No detailed analysis of expected Sentinel-4 NO_2 errors is available yet. Therefore, it is assumed here that the uncertainty of individual S4 measurements is **0.7×10^{15} molec cm^{-2}** as for TROPOMI. Changes in radiance with SZA and OZA are not considered although this will affect to the NO_2 uncertainties. The focus here is on the impact of having several measurements per day, which is the unique characteristic of the S4 instrument.

3.3.4. Cloud representation

As in the case of Sentinel-5, cloud data are needed at the time, location, and spatial resolution of the simulated S4 measurements. As values are needed for hourly simulations, the cloud data has to come from a geostationary instrument, in this case SEVIRI. The approach taken here is to use SEVIRI cloud optical thickness data and establish a link to OMI O_2-O_2 cloud fractions. As a first step, a composite of SEVIRI data has to be created using the closest measurement to the OMI overpass. For simplicity, this is done on gridded data. As SEVIRI data is hourly and no information is available on the exact timing of measurements, a temporal mismatch of +/- 30 minutes exists between the SEVIRI composite and OMI data. As shown in Figure 3.13, there is qualitative agreement between the spatial distribution of OMI cloud fractions and SEVIRI COT, but also a lot of differences in the details.

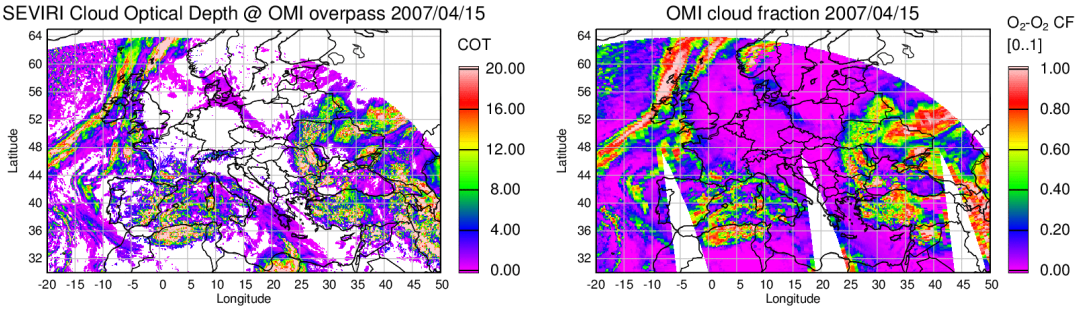

Figure 3.13: comparison of SEVIRI cloud optical thickness (left) and OMI cloud fraction (right), both for April 15, 2007. SEVIRI data are taken at the time closest to OMI overpass. White areas are regions without data.

This is further illustrated in Figure 3.14, where a two-dimensional histogram of the distribution is shown. If data is averaged into cloud optical thickness bins of 0.5, a smooth and systematic correlation between the two quantities is found (see Figure 3.14). The relation is not linear and shows some variation when varying the day within a month, probably as result of changes in the cloud statistics (Figure 3.14 middle). Also, there are some variations with season (Figure 3.14 right), again as result of statistics but possibly also because of changes in observation geometry.

As such a comparison has a lot of uncertainties, and in order to simplify the following analysis, it was decided to use the SEVIRI data only for cloud clearing, and to apply a constant threshold of cloud optical thickness of 2 to select for cloud free scenes. This

corresponds to cloud fractions of 0.2 – 0.3 according to the comparisons shown in Figure 3.14.

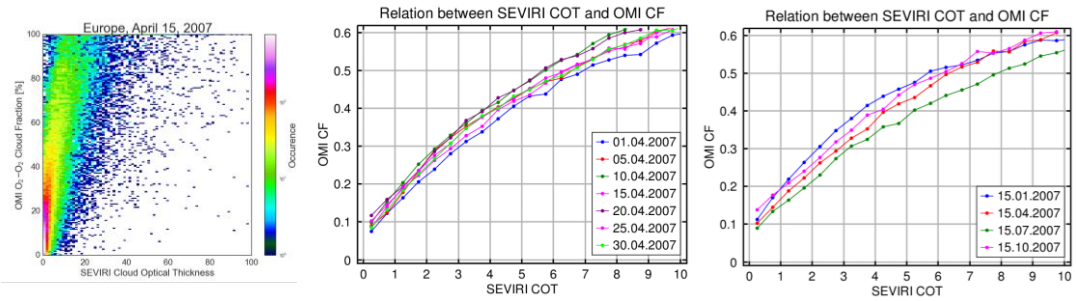

Figure 3.14. Scatter plot (left) and averaged comparison of SEVIRI cloud optical thickness and OMI cloud fraction. In the middle, results are shown for several days in April 2007, in the right figure results for one day in January, April, July, and October 2007.

When applying the SEVIRI cloud optical thickness for the S4 simulations, a problem arises from the difference in maximum accepted solar zenith angle. According to our tests, SEVIRI COT data are only supplied for SZA < 70°. This is illustrated in Figure 3.15, where the SEVIRI coverage is shown for some time steps on January 15. It is clear that the North Sea area is never covered, and also the Bay of Biscay region is only covered around noon. Comparison with Figure 3.10 shows that this is in contrast to S4 coverage using the SZA and OZA thresholds as selected, and application of SEVIRI data for cloud screening would strongly affect the statistics of the S4 simulation. It therefore was decided not to use January data.

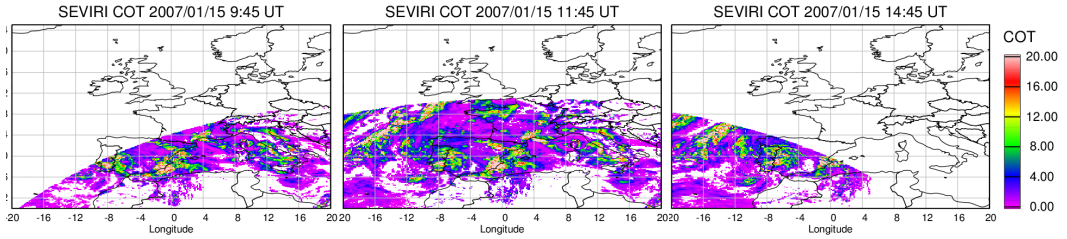

Figure 3.15: Coverage of SEVIRI COT on January 15. The North Sea area is never covered, the Bay of Biscay area only around noon

4. Sensitivity study for future sensors

4.1. Sentinel-5

4.1.1. Impact of the spatial resolution

TROPOMI has a sampling of 7×7km² at nadir with a small variation of the pixel size (factor of 2 maximum) across the swath, owing to the use of a variable binning factor (see section 3.2.2). In contrast the size of an OMI pixel varies from 13×24km² at nadir to 13×128km² for the extreme viewing angles at the edges of the swath. Compared to NO_2 VCDs simulated by the CHIMERE CTM (Figure 4.1 a), the NO_2 distribution at OMI resolution (Figure 4.2 b) appears to be smoother over the ship tracks, especially for pixels at the edge of the OMI swath. On the contrary, the difference with NO_2 maps at TROPOMI resolution is very small, since the spatial resolutions of TROPOMI and CHIMERE are very similar. In order to quantify the improvement due to the higher spatial resolution of TROPOMI, we calculated monthly gridded maps of simulated NO_2 columns at GOME-2, OMI, and TROPOMI resolutions. As can be seen in Figure 4.3, monthly averaged maps at GOME-2/OMI resolution smooth the shipping NO_2 signals by 33%/17% over EMS, and 56%/24% over BB.

It should be noted that this difference strongly depends on the of the grid size. For example, the above analysis is based on a 0.0625°×0.0625° grid, and the improvement reduces to 24%/12% and 40%/18% when changing the size of gridding cell to 0.25°×0.25°. The improvement is expected to be larger for ship tracks in south-north direction (such as the ship lane over BB), because of the larger improvement for the TROPOMI pixel size in the across-track direction.

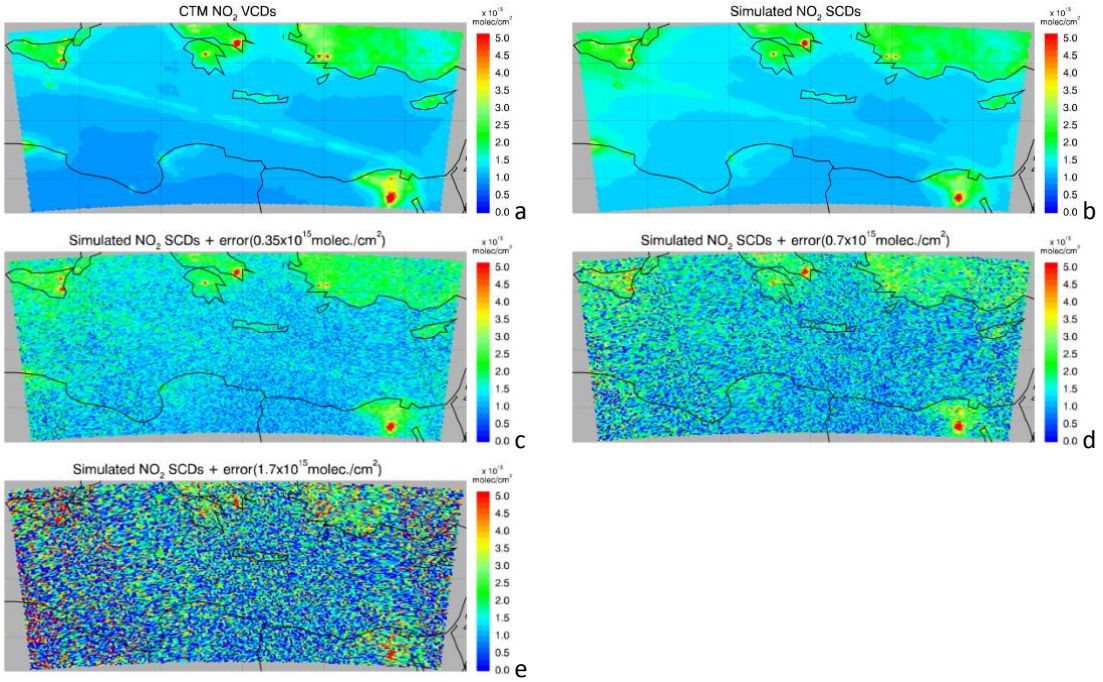

Figure 4.1: Simulated NO_2 over East Mediterranean Sea for TROPOMI. a) NO_2 VCDs for an orbit of TROPOMI observation (corresponding to OMI observation: July 7, 2007, orbit number: 15832) b) corresponding NO_2 SCDs; and simulated SCDs with a single measurement uncertainty of c) 0.35, d) 0.7, e) 1.7×10^{15} molec cm^{-2} at nadir. The error is increased by a factor of $\sqrt{2}$ and 2 for binning factors reduced by a factor 2 and 4 the at higher swath viewing angle of TROPOMI measurements.

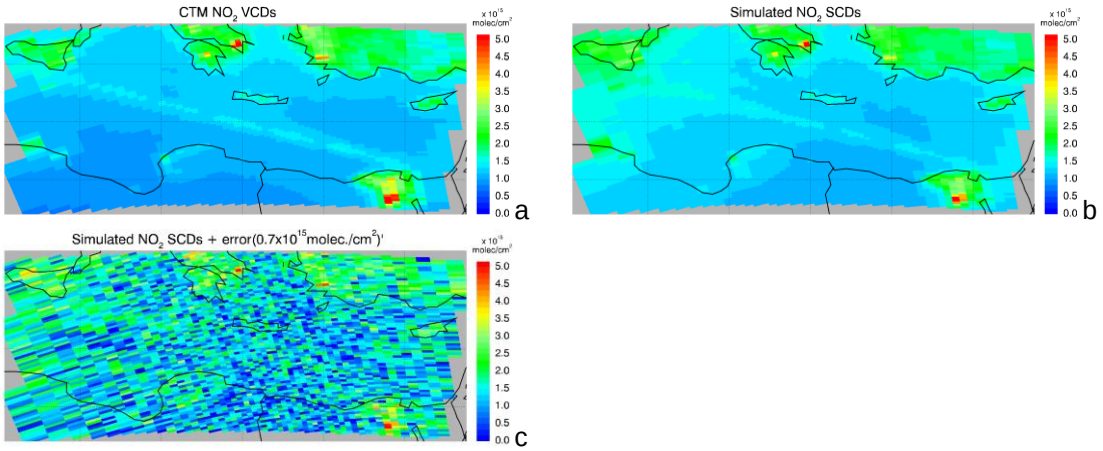

Figure 4.2: Simulated NO_2 maps for OMI. a) NO_2 VCDs for an orbit (orbit number = 15832) of OMI; b) corresponding NO_2 SCDs; c) simulated SCDs for a typical OMI error (STD=0.7×10^{15} molec cm^{-2} for individual pixels).

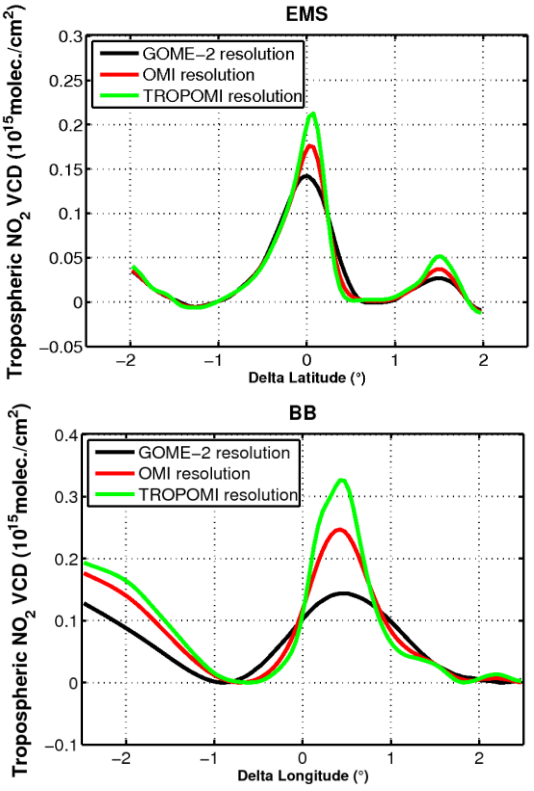

Figure 4.3: Along ship track monthly average (over the longitude 17.5°–28.5°E for EMS and over latitude 44.5°–48.5°N for BB) of tropospheric NO_2 columns simulated for the spatial resolution of GOME-2, OMI and TROPOMI observations over EMS (top) and BB (bottom), data analysis is based on monthly averages of NO_2 from CHIMERE in July. A linear background fit was subtracted from the averages.

4.1.2. Improvement of the error on NO_2 SCDs

Figure 4.1 and Figure 4.2 illustrate step by step the NO_2 simulation approaches used for TROPOMI and OMI observations. Figure 4.4 gives the monthly average maps of simulated NO_2 VCDs for July for the different cases of the simulation. For simplification, we assume the true NO_2 distribution is invariable (monthly average for July) and in completely cloud-free condition, but the geolocation of ground pixels and the solar position vary with the satellite

observations (as described above for OMI and the corresponding TROPOMI measurements). A simple AMF for an albedo of 0.06 and a 1.5km thick layer of NO_2 in the boudary layer is used to convert the simulated SCDs into VCDs. All datasets are gridded at 0.125° × 0.125° spatial resolution, and are then averaged over a month. Additionally a spatial high pass filter was applied to monthly averaged maps to enhance the NO_2 signal from the shipping lane. The NO_2 VCDs from ship emissions over EMS are on the order of $0.2–0.4\times10^{15}$molec cm^{-2} (Figure 4.4 a).
Simulated TROPOMI observations corresponding to SCD errors of 0.35×10^{15} and 0.7×10^{15} molec cm^{-2} can clearly identify a NO_2 signal over the ship track, while in case of larger noise (error of 1.7×10^{15} molec cm^{-2}) the NO_2 signal can hardly be seen. However, if the pixel size is increased by binning (such as illustrated in Figure 4.4 f), the noise of the NO_2 map is reduced and the shipping lane becomes clearer. This highlights the importance of the SNR for the detection of shipping lanes.

Table 4.1 and Table 4.2 summarise the errors of monthly mean NO_2 column data corresponding to different error levels for individual pixels and different spatial gridding scenarios. The shipping NO_2 values corresponding to different resolutions are also listed. This analysis is based on the improved gridding algorithm described in WP 2000. The following conclusions can be drawn:

a) Monthly errors show a linear correlation with individual pixel errors.
b) The error is reduced when the size of the grid increases. This reduction is small when the grid size is smaller than the size of satellite pixels. Errors will be reduced by 40%-50% when the grid size increases by a factor of 4, if the grid size is larger than the satellite pixels.
c) NO_2 peaks show a similar spatial resolution dependence as the errors.
d) The errors from OMI simulation are smaller than the errors from TROPOMI simulations for equivalent error level (TROPOMI 1.7×10^{15} vs. OMI 0.7×10^{15} molec cm^{-2}). If TROPOMI pixels are binned by 2×3, the errors are reduced by 10–30%.
e) For TROPOMI NO_2 columns having errors of 0.7×10^{15} molec cm^{-2} on individual pixels, shipping NO_2 lanes will be detectable over EMS in 8/6-day averages at a 0.125°/0.25° grid, coarser resolution requiring a smaller number of days. The errors are reduced by a factor of 2 in comparison to OMI observations. As discussed in WP 2000 (Figure 10 case 2), the shipping NO_2 signal over BB/NS ($0.18/0.075\times10^{15}$ molec cm^{-2}) is 64% larger/32% smaller than the shipping NO_2 over EMS (0.11×10^{15} molec cm^{-2}). Hence, the shipping NO_2 will be visible for the average of approximately 3/30 days of TROPOMI observations.
f) If integrated along the ship track, the NO_2 STD is reduced by approximately a factor of 10, so one day of data is enough to detect the shipping signal for all cases over EMS. The improvement of the SNR is expected to be smaller over BB and NS due to the relatively short length of ship track (~1000km for EMS versus ~500km for BB and ~200km for NS).

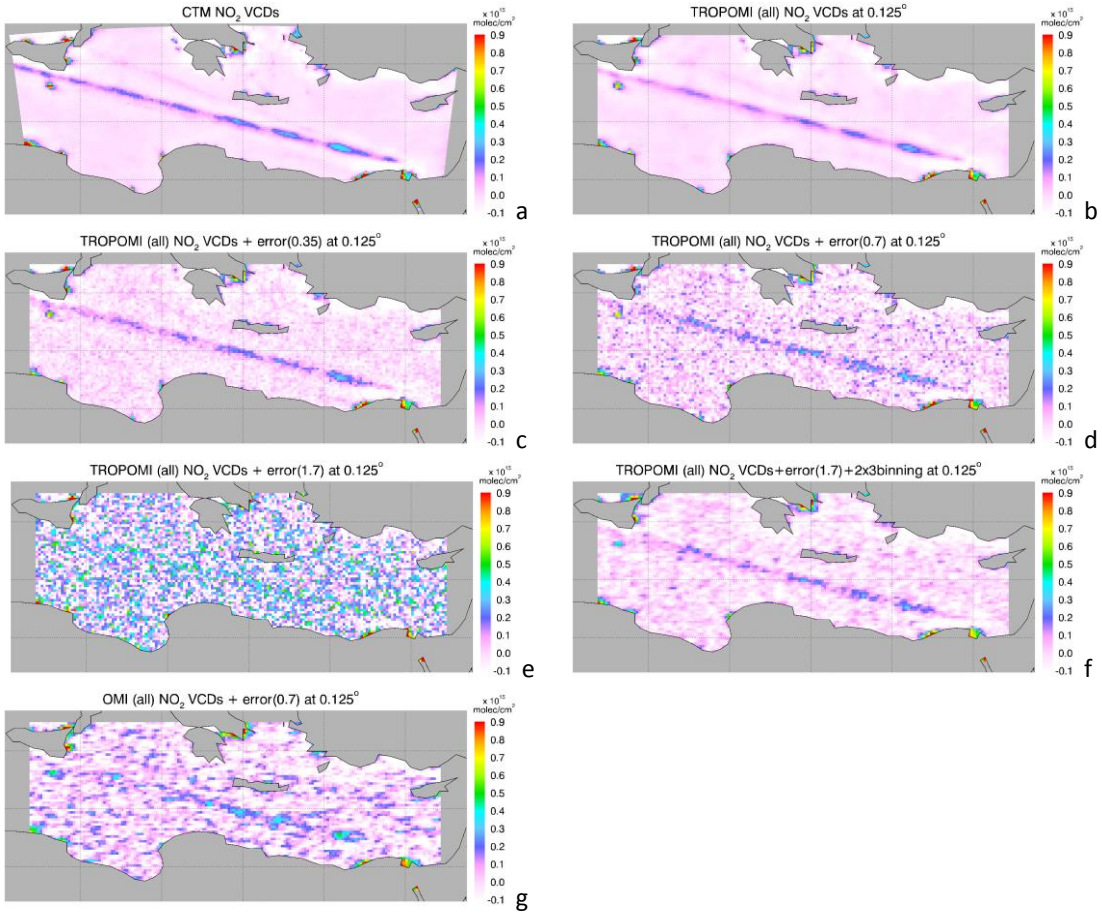

Figure 4.4: Monthly average (July 2007) of tropospheric NO_2 columns derived from the different scenarios: a) NO_2 VCDs from CHIMERE output; b) Simulated for TROPOMI observation; c)-e) Simliar to b), but with 0.35, 0.7 and 1.7×10^{15} molec cm^{-2} error of SCDs for individual pixels at nadir respectively; f) similar to d), but binning 2×3 TROPOMI pixels; and g) OMI simulation with 0.7×10^{15} molec cm^{-2} error of SCDs for individual pixels. A simple AMF for an albedo of 0.06 and a 1.5km thick layer of NO_2 in the boudary layer is used for b)-g) to convert SCDs into VCDs. Data have been spatially high pass filtered to highlight the signals from ship emssion, map gridded at 0.125°×0.125°.

Table 4.1: Standard deviation (STD) of the differences of monthly (July) NO_2 VCDs simulated with and without errors, and corresponding NO_2 peak averages (Figure 4.4b) for the ship track over EMS at different spatial resolutions (Units: 10^{15} molec cm^{-2}).

Grid cell	TROPOMI (0.35)	TROPOMI (0.7)	TROPOMI (1.7)	OMI (0.7)	NO_2 peaks over EMS ship track
0.0625°	0.067	0.138/0.096*	0.328	0.165	0.195/0.169**
0.125°	0.046	0.093/0.084*	0.228	0.147	0.183/0.164**
0.25°	0.031	0.069/0.058*	0.157	0.117	0.155/0.140**
0.5°	0.015	0.030/0.034*	0.074	0.076	0.093/0.087**

*The later values are the results of binning 2×3 of TROPOMI pixels.

** values are averages for TROPOMI/OMI pixels

Table 4.2: Same as Table 4.1, for monthly NO_2 integrated over ship track. (17.5°–28.5°E for EMS).

Grid cell	TROPOMI (0.35)	TROPOMI (0.7)	TROPOMI (1.7)	OMI (0.7)
0.0625°	0.0069	0.0117/0.0098	0.0245	0.0190
0.125°	0.0056	0.0082/0.0070	0.0170	0.0161
0.25°	0.0047	0.0066/0.0053	0.0122	0.0133
0.5°	0.0025	0.0036/0.0032	0.0068	0.0072

4.1.3. Cloud effect

Since UV-visible instruments are limited in spatial resolution, only a few percent of the pixels are completely cloud free, so most of pixels are generally affected by clouds. Clouds can shield trace gases from observation, but they can also enhance the sensitivity to trace gases when present above clouds. Furthermore, the presence of clouds will affect the photochemical/heterogeneous reaction of nitrogen oxides that change the lifetime and concentration of NO_2. The distribution of cloud amount over European waters and the effect of clouds on NO_2 observations from satellite has been discussed in WP 2000. Generally, there are more cloud-free scenes over low latitudes than high latitudes, and the hot season is less cloudy than the cold season, and both GOME-2 and OMI cloud algorithms show a significant impact on the NO_2 retrieval.

Here, we simulate NO_2 for TROPOMI and OMI observations using CHIMERE data, and cloud properties from the MODIS product are used to calculate AMFs based on the indpendent pixel approximation (Stammes et al., 2008) approach. First, the number of cloud-free days is investigated based on the criteria of cloud fraction less than 30%. Figure 4.5 shows the fractions of the cloud-free pixels based on the MODIS cloud product for OMI and TROPOMI pixels over EMS, BB and NS regions. Compared to OMI, TROPOMI measurements slightly increase the number of cloud-free pixels, and this difference is relatively large during winter when most areas are covered by cloud. The effect of clouds on the NO_2 retrieval is investigated by comparing the tropospheric AMF with and without cloud correction (namely, the AMF for the completely clear scene, AMF_{clear}). In this case, CHIMERE profiles are used for AMF calculation. Figure 4.6 shows the ratio of AMF and AMF_{clear} as the function of the cloud fraction. Generally, AMF is smaller than AMF_{clear}, the shielding effect dominates. The effect of clouds increases with cloud fraction, and clouds reduce the NO_2 signal by up to 35% in the case of cloud fractions below 30%, but the difference of the cloud effect between OMI and TROPOMI observations is negligible.

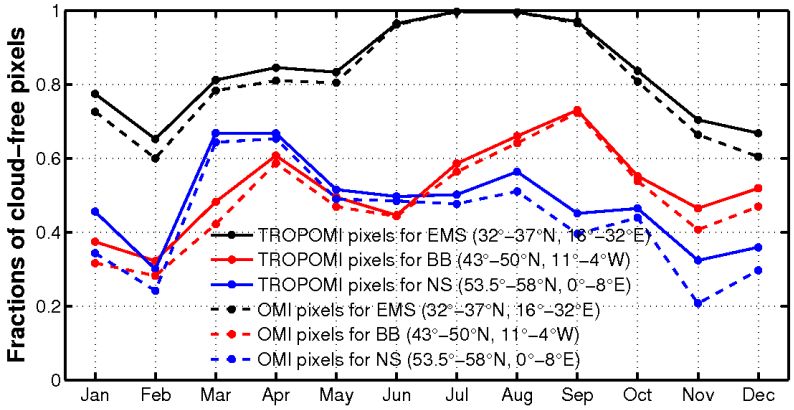

Figure 4.5: Statistic of cloud free pixels from satellite measurements over three selected European ship track areas (EMS, BB and NS). The analysis is based on CHIMERE data simulated for TROPOMI and OMI observations, and cloud properties are taken from the MODIS product. Results for OMI include an area weight to account for the variable pixel size. Satellite observations with sun glint geometry are excluded from the analysis.

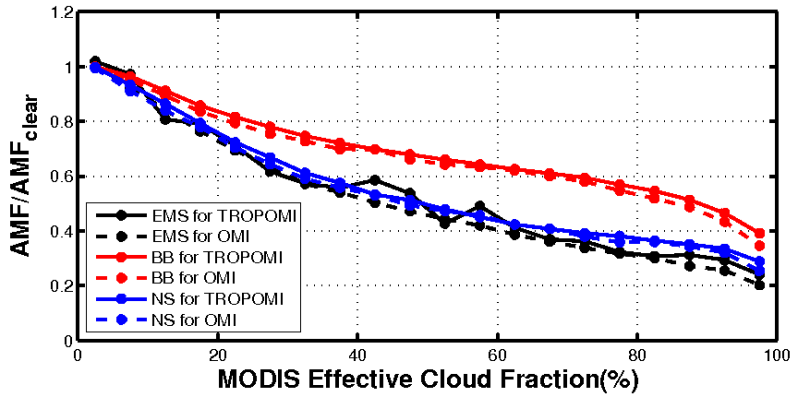

Figure 4.6: Ratio of AMF including cloud correction and AMF for the clear scene as a function of effective cloud fraction. The simulation for OMI and TROPOMI observations is based on four months (January, April, July and October 2007) of the CHIMERE NO_2 data, and cloud properties are taken from MODIS cloud product.

4.1.4. Wind effect

As discussed in WP2000, meteorology has a strong seasonal variation over European waters. For shipping NO_2 detection, strong winds will lead to dispersion of the NO_2 plume emitted in the ship track, making its detection difficult. Figure 4.7 counts the number of calm wind days (defined as wind speed at 12:00LT less than 5m/s) for three selected areas in different seasons, based on a 6-year (2005-2010) ECMWF data record. Results show that there are up to 47%/32%/30% of days having low wind conditions over the EMS/BB/NS areas, and more windy days in winter than in summer. It should be noted that, as discussed in WP 2000, the effect of wind on the detection of the shipping signal needs to be combined with the lifetime of NO_2. A shorter lifetime of NO_2 (such as at low latitudes during summer) leads to less dispersion of shipping NO_2 plumes, and the threshold of wind speed for the definition of calm wind days can be larger for this case; whereas the threshold of wind speed should be smaller at high latitudes (such as NS) in winter due to the relatively long lifetime of NO_2. If a wind speed less than 7.5m/s and 2.5m/s is defined as a calm wind day for the case of shorter and longer lifetime of NO_2, respectively, as shown in Figure 4.7, there are more than 70% of days having good weather conditions for the detection of the shipping signal over EMS in summer, whereas less than 10% of the days are considered as good over BB/NS in winter.

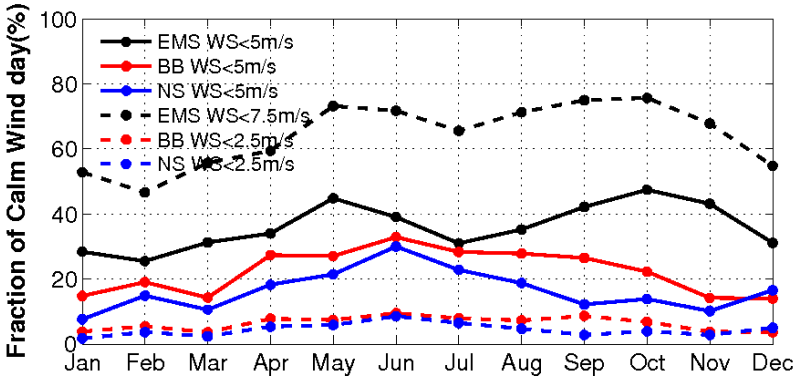

Figure 4.7: Monthly percentage of calm wind days over EMS, BB and NS. The calm wind days are defined as days having wind speed at 12:00LT less than 5m/s, and the number of days with wind speed below 7.5m/s and 2.5m/s for the case of EMS and BB/NS is also shown in the figure. Analysis is based on six years (2005-2010) of ECMWF data.

4.1.5. Sun glint effect

Over European waters, sun glint geometry mostly occurs at low latitudes (namely, over the Mediterranean Sea). There are 15% of TROPOMI observations from May to July (Figure 4.8) affected by sun glint. As discussed in WP2000, the satellite observed NO_2 columns with sun glint geometry are enhanced by a factor of 2 over EMS. On average, the shipping NO_2 signal increases by about 15% (≈15%×2 + (1−15%)×1 − 100%) due to the effect of sun glint over the EMS area.

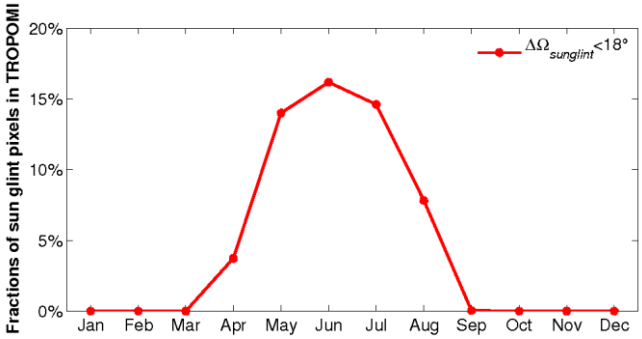

Figure 4.8: Percentage of pixels affected by sun glint from TROPOMI observations over EMS.

4.2. Sentinel-4

In order to evaluate the detectability of shipping NO_2 in S4 geostationary observations, the following steps have been performed

1. Computation of hourly NO_2 slant columns using box AMFs from SCIATRAN and NO_2 vertical profiles from CHIMERE.
2. Re-gridding of the model data to the S4 spatial resolution and projection, resulting in grid cells of about 0.1° longitude and 0.07° latitude in the Bay of Biscay region.
3. Cloud filtering using SEVIRI observations and the transfer from cloud optical thickness to cloud fraction as explained in section 3.3.4 with a threshold of 2 COT.
4. Integration of hourly data to daily fields
5. In some cases, integration of plume transects along shipping tracks

Originally, the analysis was planned for the three selected regions (North-Sea, Bay of Biscay, and Eastern Mediterranean) and for the four months with model data (January, April, July, and October). However, due to some limitations, not all cases could be fully evaluated:

1. In the North Sea model data, ship tracks do appear to be misplaced in some regions and are not in agreement with OMI observations. It was therefore decided to not analyse these data further. In the context of S4, this region also suffers from relatively large observation angles which will increase uncertainties of the retrievals.
2. As discussed in section 3.3.4, SEVIRI cloud data are not available for all simulated S4 pixels in winter. Therefore, data from January could not be included in the full analysis.
3. In the Mediterranean, there is a large data gap in the model data in July and thus days were repeated for the statistical analysis performed on the July data in this region.

4.2.1. Detectability of monthly shipping NO_2 signals

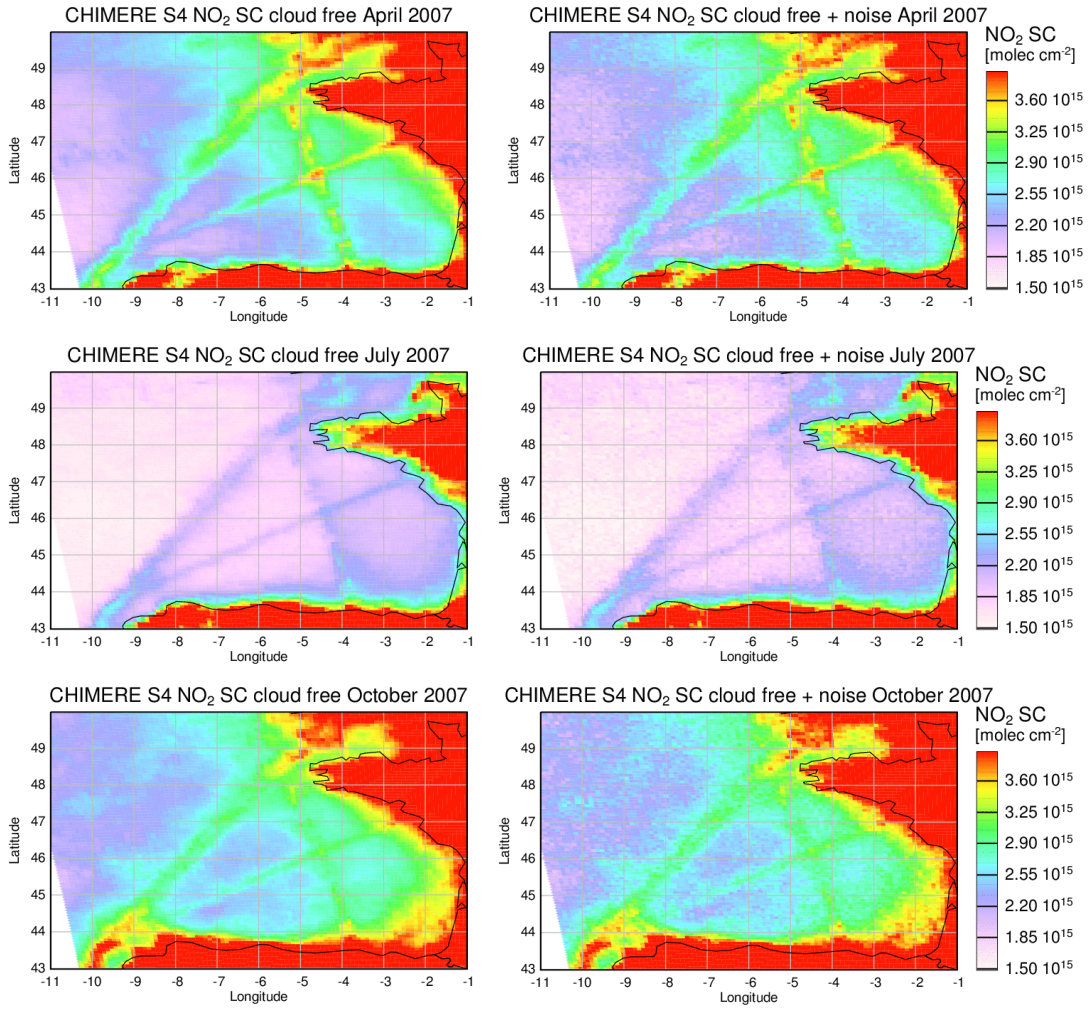

Figure 4.9: Monthly averages of cloud free simulated S4 NO_2 slant columns for the Bay of Biscay. Left column is without noise, right column with Gaussian noise assuming a single measurement uncertainty of 0.7×10^{15} molec cm^{-2}

In monthly averages of simulated clear sky S4 observations without noise, shipping signals in the Bay of Biscay are clearly discernible. Detectability of these signals depends on the noise in the measurements and the absolute number of observations. As S4 takes hourly data, the number of measurements per simulated grid cell is much larger than for low earth observations such as from S5. How many clear observations per month there are is shown in Figure 4.10: In April, there are between 120 and 200 observations per pixel, in July more than 170 and in October between 100 and 150. Assuming Poisson-Statistics, this would reduce the

assumed measurement uncertainty of $0.7x10^{15}$ molec cm^{-2} for individual measurements by a factor of 10 – 14 to 0.05 – $0.07x10^{15}$ molec cm^{-2}. This is visualised in the right part of

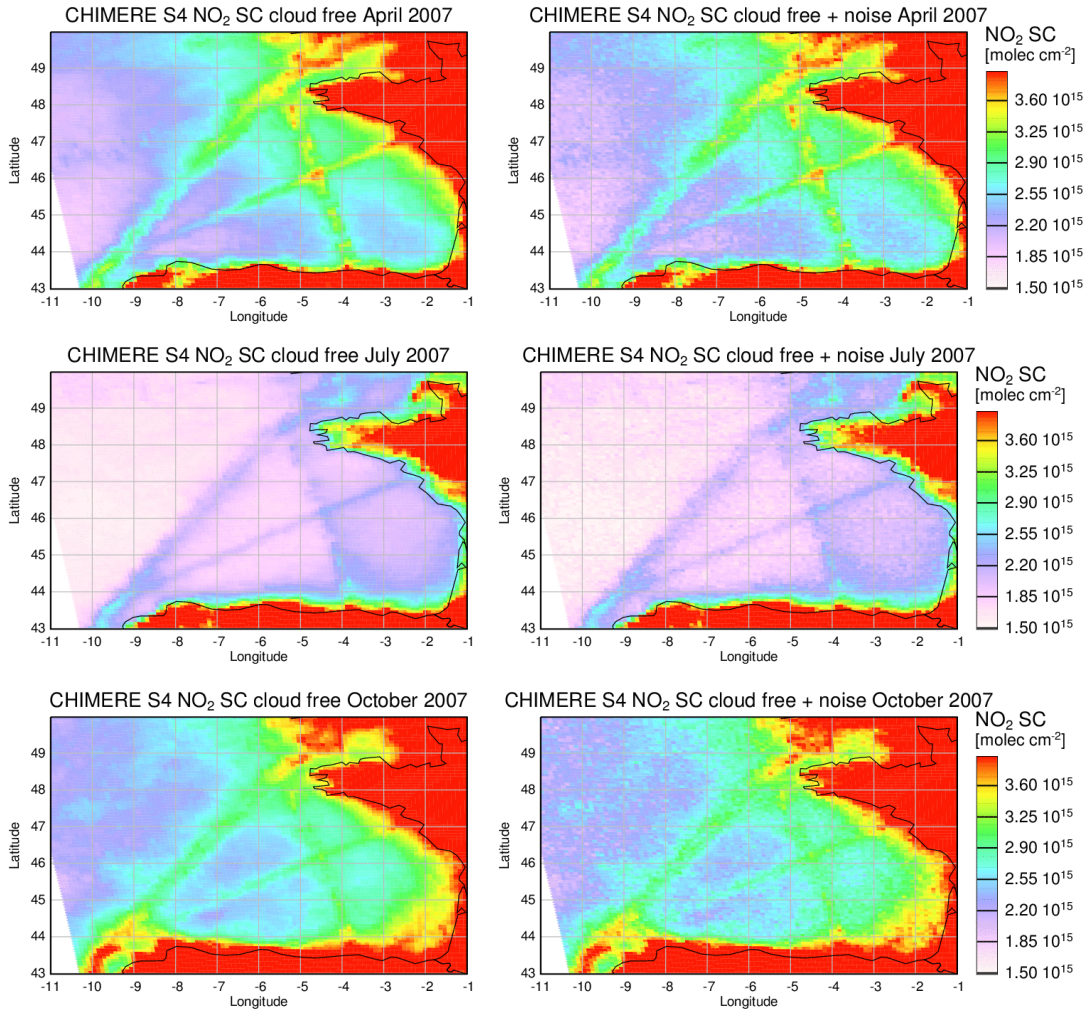

Figure 4.9, where Gaussian noise with a sigma of $0.7x10^{15}$ molec cm^{-2} has been added to each individual measurement. As result of the large number of measurements obtained from geostationary orbit, the noise in daily or monthly aggregates is much smaller than for instruments such as OMI or TROPOMI and certainly does not prevent detection of shipping NO_2 in the bay of Biscay in monthly averages.

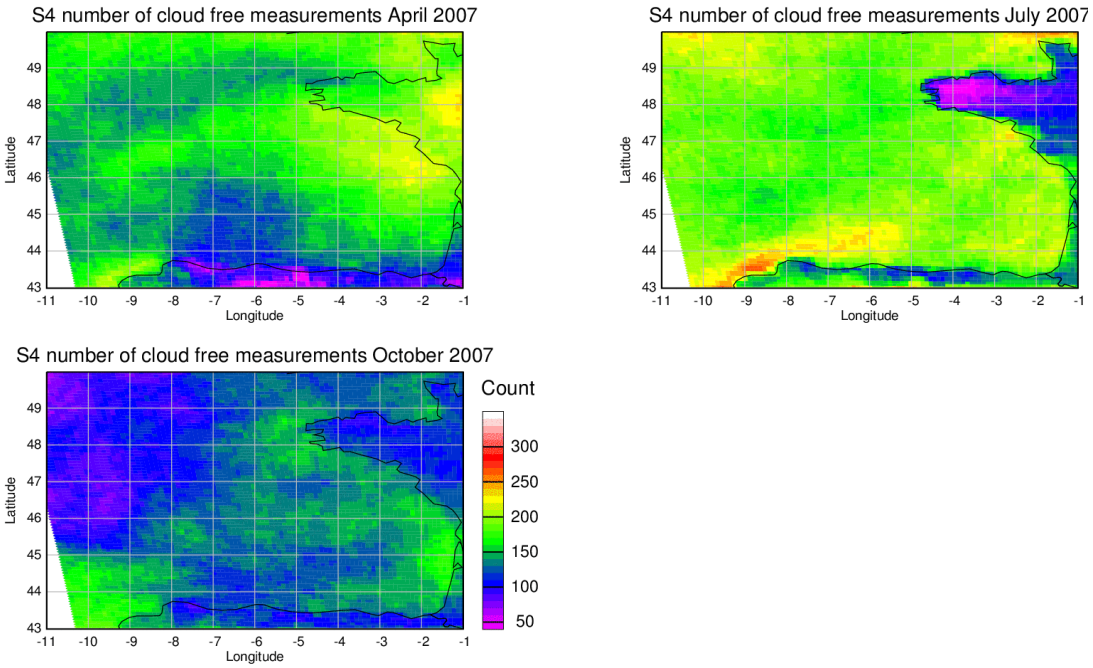

Figure 4.10: Number of monthly S4 observations with SEVIRI cloud fraction < 0.3 in the Bay of Biscay

The averaging reduced uncertainty has to be compared with the contrast in NO_2 values between regions inside and outside the shipping lanes. As can be seen in the values integrated along the ship track as shown in Figure 4.11, the enhancement in the ship track is between $0.3x10^{15}$ molec cm^{-2} and $0.6x10^{15}$ molec cm^{-2}, depending on season. Thus, uncertainties of individual grid cells in S4 observations are nearly one order of magnitude smaller than the expected signal, making visual detection of shipping NO_2 possible in monthly averages. As discussed in section 4.1.1, further improvement is possible by reducing the spatial resolution if at all necessary. When looking at results integrated along the ship track, another factor of 50 in the number of observations or 7 in reduction of uncertainty can be obtained, bringing the random error in monthly integrated NO_2 shipping signals down to just a few per cent (see Figure 4.11 right).

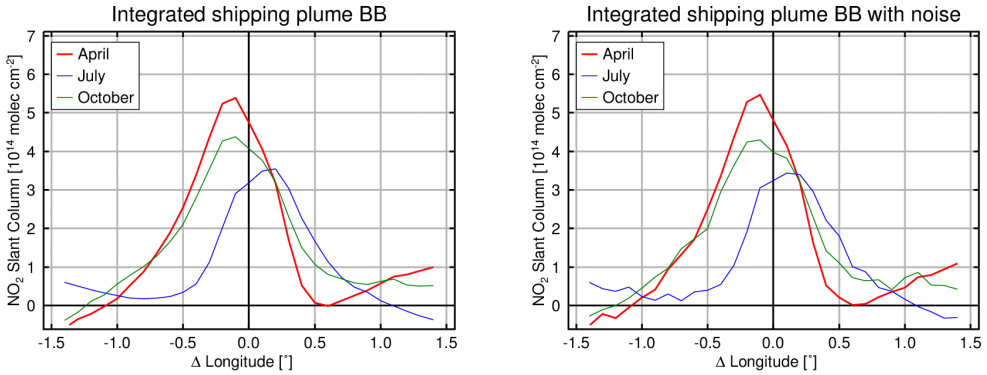

Figure 4.11: Cross-section through simulated monthly clear data S4 shipping plume in the Bay of Biscay, integrated along the plume between (44.4°N, 9°W) and (48.2°N,6°W). Left figure is without noise, right figure with noise.

The same analysis as for the Bay of Biscay has been performed for the Eastern Mediterranean region. As for technical reasons some days of model data were missing, in particular in July, these data were replaced by repeating other days of the month. While this

could potentially introduce a bias in the analysis, it is considered acceptable for the rough estimates made here.

In comparison to the Bay of Biscay, the Mediterranean has more cloud free observations and somewhat more favourable observation geometry (smaller SZA and OZA). The total (cloudy and clear) number of S4 observations in summer is however somewhat lower because of shorter day length. Another difference is the lifetime of NO_2 which is shorter in the Mediterranean, leading to smaller NO_2 signals from ships but less smearing of the ship tracks through transport.

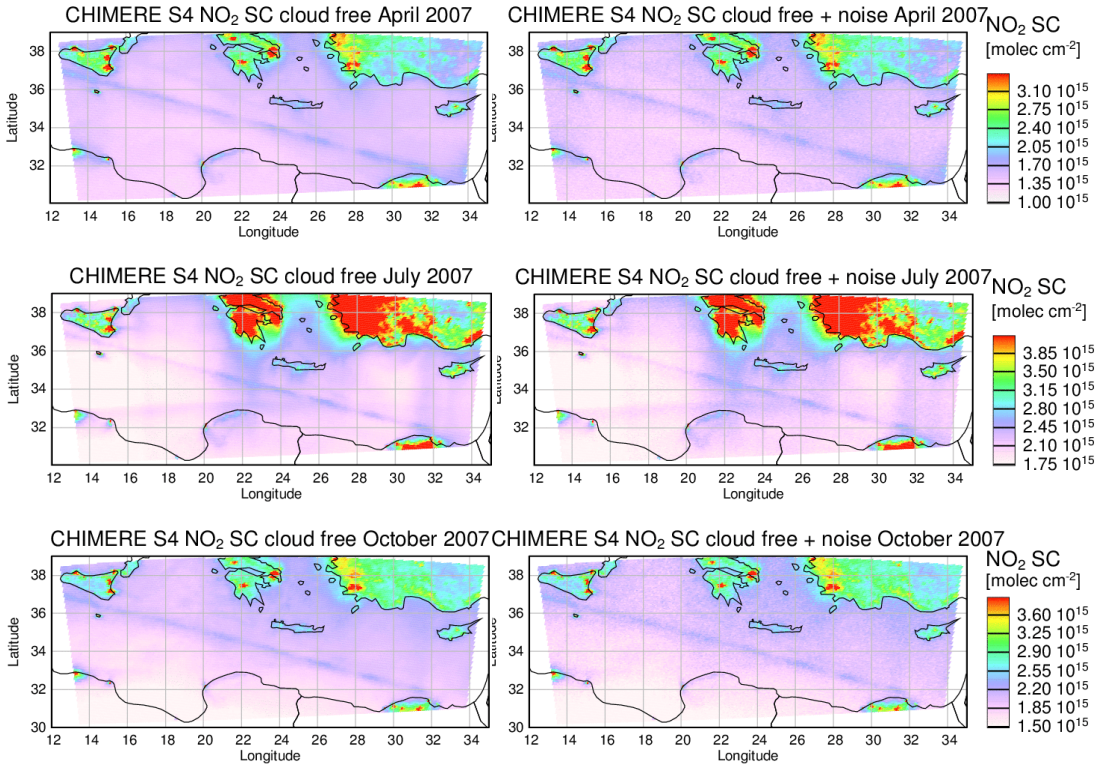

Figure 4.12: Monthly averages of cloud free simulated S4 NO_2 slant columns for the Eastern Mediterranean. Left column is without noise, right column with Gaussian noise assuming a single measurement uncertainty of 0.7×10^{15} molec cm^{-2}. Please note the change in colour scale between months. July data are based on a small number of days which have been repeated to obtain appropriate number of measurements.

As can be seen in Figure 4.12, the shipping signal can be clearly seen in monthly simulated S4 data. Because of the large number of observations, the noise which is larger than the shipping signal in individual observations can hardly be seen in monthly averages.

How well the NO_2 from ships can be detected in monthly simulated S4 data is demonstrated in Figure 4.13 where the latitudinal cross-section of the plume in the Eastern Mediterranean is shown with and without noise for the three months. Clearly measurement noise plays only a small role in the data when averaging over as many measurements as done here.

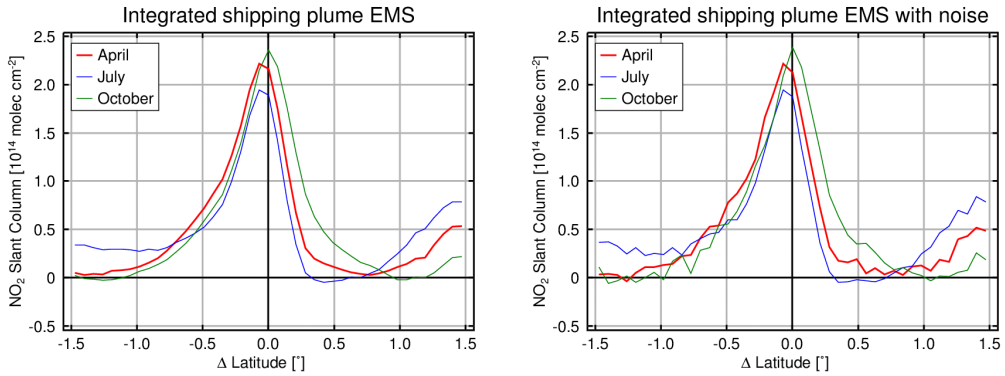

Figure 4.13: Cross-section through simulated monthly clear data S4 shipping plume in the Eastern Mediterranean, integrated along the plume between (36.2°N, 16°E) and (32.6°N, 32°E). Left figure is without noise, right figure with noise.

While the repeated measurements of S4 during the day help to improve the statistics of the ship plume measurements, there is a problem with the diurnal variation in NOx photochemistry. During the day, NO_2 values change and by creating a composite image from different time slices, artificial structures are introduced into the daily and to lesser degree even the monthly maps. For a quantitative analysis, this will have to be considered by explicit modelling of the observations using a regional model. Such an approach of course relies on the model's ability to realistically represent the diurnal variation of NO_2 in the troposphere over the ocean.

4.2.2. Detectability of daily shipping NO_2 signals

Detectability of shipping signals on daily basis would be preferable over monthly values. In how far this is feasible depends on a number of different parameters:

- The number of cloud free measurements possible along the shipping lane
- The amount of land-based pollution which is blown towards the open ocean, masking the shipping signal
- The wind speed and NO_2 life time which determines the contrast of the shipping NO_2 plume above the background

In Figure 4.14, four days in April 2007 are shown illustrating the variability. While a clear shipping signal can be seen on April 12, hardly any measurements are available on April 16 and large other pollution signals mask the shipping lane on April 3. On April 19, there is a clear shipping signal but the plume is less well confined as on April 12. From these examples it is clear, that even with a perfect instrument, shipping signals in the Bay of Biscay cannot be detected on each day with the naked eye.

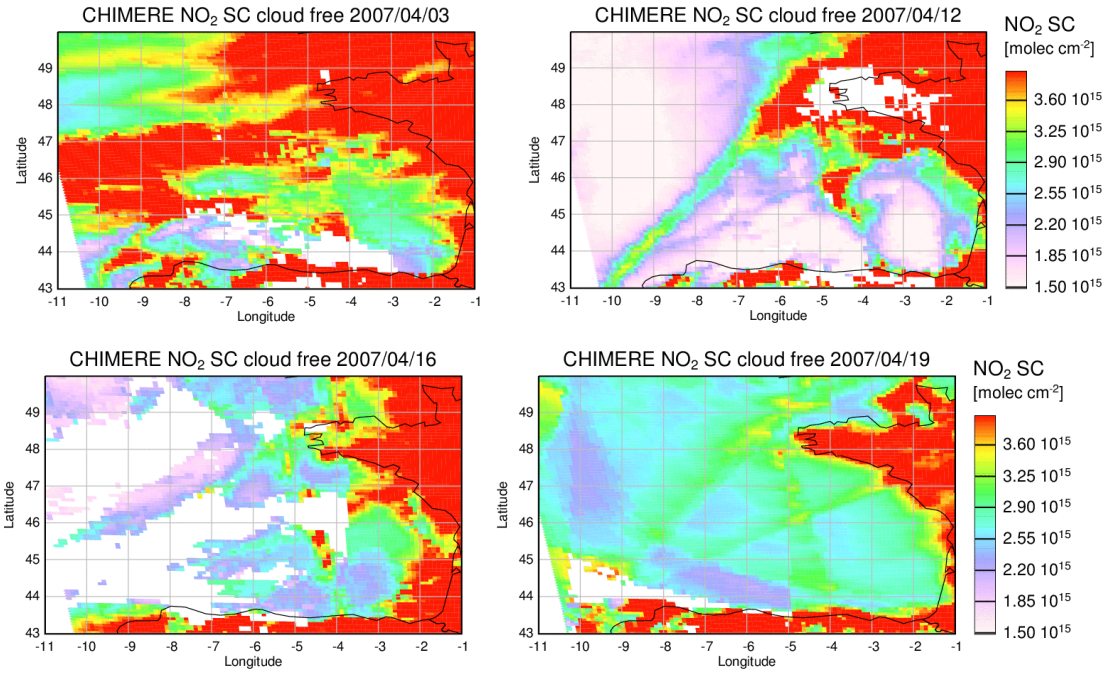

Figure 4.14: Four example days of S4 NO_2 slant columns simulated by CHIMERE for individual days in April 2007. Only data flagged as cloud free by SEVIRI have been used. White areas are regions without cloud free observations.

However, by integrating along the ship track and removing the background signal, the signal to noise can be much improved and as shown in Figure 4.15, for all four days there is a clear maximum around the shipping lane when integrating along the track. The exact position varies from day to day according to wind direction and speed. At the same time, absolute values also vary considerably, which is not the result of changes in NO_x emissions by ships, but rather a combined effect from variations in photochemistry, transport and data sampling due to clouds.

In order to judge the detectability by the real S4 instrument, the assumed uncertainty of an individual measurement (0.7×10^{15} molec cm^{-2}) and the number of measurements need to be taken into account. The resulting uncertainties are indicated as shaded area in Figure 4.15. As can be seen, the shipping signal is in all cases above the detection limit for the integrated signals. This is the result of the large number of observations available from the good spatial resolution and the hourly measurement cycle.

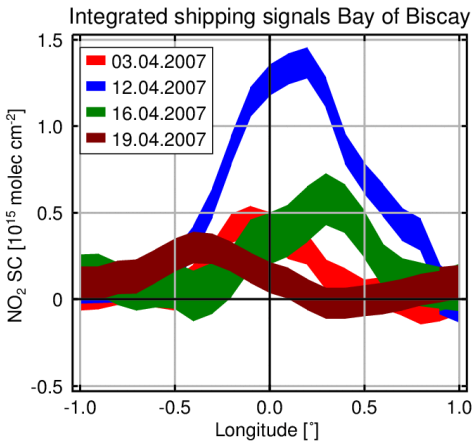

Figure 4.15: NO_2 shipping signal integrated along the ship track in the Bay of Biscay for the four days shown in Figure 4.14. The shaded area is the uncertainty computed from the number of values used for each 0.1° longitude bin and the assumed measurement uncertainty for S4. A linear background has been subtracted from each curve.

In real data, additional uncertainties not included here (aerosols, cloud effects even in those pixels having cloud fractions smaller than 0.3, variations in surface reflectivity depending on wind speed, instrumental issues) will increase the errors. Also, the current analysis relies on CHIMERE model results which might not be fully representative of the real atmospheric situation. However, it can be expected that on many days, S4 will provide daily values for the integrated shipping NO_2 in the Bay of Biscay and the Mediterranean.

5. Summary

5.1. Sentinel-5

We created pseudo-observation datasets for the S5P based on data from the high resolution CHIMERE chemical transport model. The geometry and geolocation of TROPOMI observations are simulated by extrapolation of OMI data, and cloud parameters are taken from the MODIS cloud products. Moreover, meteorological data fields from the ECMWF reanalysis are used to investigate wind effects on the NO_2 distribution.

The following conclusions are reached:

A. Owing to its higher spatial resolution compared to OMI, TROPOMI measured NO_2 peaks from the narrow shipping lanes will be 17%(EMS)/24%(BB) higher, and the improved SNR will reduce up to 50% of noise level on TROPOMI NO_2 maps.
B. The detection of a shipping NO_2 signal requires at least a few days of TROPOMI measurements. However if integrated along the ship track, the SNR will improve by up to a factor of 10, and detection could be achieved in daily maps. Furthermore, the NO_2 signal from shipping lanes will be more easily detected after suitable binning of TROPOMI pixels, owing to noise reduction at the typical scale of the shipping plumes (broader than TROPOMI pixels).
C. Clouds and meteorology are as important as SNR over BB and NS areas, in particular during the cold season, when strong wind and cloudy scenes often happen. In addition, since the atmospheric lifetime of NO_x is longer and the SNR lower due to prevailing low solar zenith angles, it is difficult to detect shipping NO_2 over these regions.
D. Observations under sun glint geometry increases the shipping NO_2 signals by 15% on average for TROPOMI over EMS during the summer time.

5.2. Sentinel-4

Measurements of the geostationary S4 instrument were simulated using high resolution CHIMERE NO_2 fields, the current specification of the instrument, and dedicated radiative transfer calculations with SCIATRAN. Cloud effects have been included using SEVIRI cloud optical thickness data where available.

The main conclusions from the simulations are

A. The observations of S4 at higher latitudes including the North Sea are performed under large observation zenith angles which will limit the sensitivity to the surface, in particular in winter
B. The improved spatial resolution as compared to GOME-2 and OMI increases the number of measurements for averaging, improving the detection of shipping NO_2
C. The hourly observations of S4 will increase the number of available measurements by about an order of magnitude, reducing the noise of the observations very much.
D. The hourly observations of S4 will also significantly reduce the areas in daily observations of ship tracks for which no data is available due to clouds
E. Monthly observations of the main shipping lanes in the Bay of Biscay and Mediterranean will have good signal to noise. When integrated along ship tracks, the random error will be of the order of a few percent, making it small compared to other sources of uncertainty in the retrievals.

F. Daily observations of shipping NO_2 appear possible when integrating along ship tracks even under unfavourable conditions

6. References

Boersma, K. F., Eskes, H. J., Dirksen, R. J., van der A, R. J., Veefkind, J. P., Stammes, P., Huijnen, V., Kleipool, Q. L., Sneep, M., Claas, J., Leitao, J., Zhou, Y., and Brunner, D.: An improved tropospheric NO_2 column retrieval algorithmfor the Ozone Monitoring Instrument, *Atmos. Meas. Tech*., 4, 1905-1928, 2011, *www.atmos-meas-tech.net/4/1905/2011/*, doi: 10.5194/amt-4-1905-2011.

Dobber, M., Kleipool, Q., Dirksen, R., Levelt, P. F., Jaross, G., Taylor, S., Kelly, T., Flynn, L., Leppelmeier, G., and Rozemijer, N.: Validation of Ozone Monitoring Instrument level 1b data products, *J. Geophys. Res.*, 113, D15S06, doi:10.1029/2007JD008665, 2008.

Levelt, P. F., van den Oord, G. H. J., Dobber, M. R., Malkki, A., Visser, H., de Vries, J., Stammes, P., Lundell, J. O. V., Heikki S.: The Ozone Monitoring Instrument, *IEEE Trans. Geosci. Remote Sens.*, 44(5), 1199-1208, 2006.

Stammes, P., Sneep, M., de Haan, J. F., Veefkind, J. P., Wang, P., Levelt, P. F.: Effective cloud fractions from the Ozone Monitoring Instrument: Theoretical framework and validation, *J. Geophys. Res.*, 113, D16S38, doi:10.1029/2007JD008820, 2008.

van Geffen, J. H. G. M., Boersma, K. F., Maasakkers, J. D., Veefkind, J. P.: TROPOMI ATBD of total and tropospheric NO_2 data products, S5P-KNMI-L2-0005-RP, 2013.

Vinken, G. C. M., Boersma, K. F., Donkelaar, K.F., Zhang, L.: Constraints on ship NOx emissions in Europe using GEOS-Chem and OMI satellite NO_2 observations, *Atmos. Chem. Phys.*, 14, 1353-1369, 2014, www.atmos-chem-phys.net/14/1353/2014/, doi:10.5194/acp-14-1353-2014.

Veefkind, J. P., Aben, I., Mcmullan, K., Forster, H., de Vries, J., Otter, G., Claas, J., Eskes, H. J., de Haan, J. F., Kleipool, Q., van Weele, M., Hasekamp, O., Hoogeveen, R., Landgraf, J., Snel, R., Tol, P., Ingman, P., Voors, R., Kruizinga, B., Vinck, R., Visser, H., Levelt, P. F.: TROPOMI on the ESA Sentinel-5 Precursor: A GMES mission for global observations of the atmospheric composition for climate, air quality and ozone layer applications. *Remote Sensing of Environment*, doi:10.1016/jrse2011.09.27, 2012.

Appendix A Meteorological and chemistry-transport modelling

A.1 Meteorological modelling

A.1.1 The WRF model

The numerical weather prediction model used in this study is the so-called Weather Research and Forecasting (WRF) model [Skamarock et al. 2008]. The WRF model is a state-of-the art regional atmosphere model developed by the National Center for Atmospheric Research (NCAR) in the United States in cooperation with many universities and other parties. The model is used by many institutes around the world, both for research and operational purposes. The model code is fully parallelised and can be used on hardware ranging from a single PC to the largest supercomputers.

The WRF model was written in a modular fashion, allowing flexible replacement and addition of different dynamics and parameterisations. The model has two ``dynamics cores'', one hydrostatic and one non-hydrostatic. At BMT ARGOSS the non-hydrostatic core is used, which can be used for a large range of spatial scales. For “real data” cases the model is typically applied to domains ranging from continental scale at resolutions of roughly 30 km down to domains with a resolution of 1 km. For “idealistic” cases the model can be used down to the scale of large-eddy simulations with resolutions of meters.

BMT ARGOSS uses the non-hydrostatic core of the model, allowing the simulation of small-scale non-stationary effects such as rapidly rising air under cumulus clouds. The model comes with a large number of physical parameterisation schemes. The model makes use of a surface layer scheme, a planetary boundary layer scheme, a cumulus parameterisation scheme for resolutions above 5 km, and a microphysics scheme allowing for the formation of ice, snow, graupel, and rain.

A.1.2 Model setup

WRF is a regional atmosphere model which means it cannot run without boundary conditions. Both the initial conditions and boundary conditions are supplied by NCEP FNL (Final Analysis) data. These data consist of analysed global fields into which most available meteorological measurements were assimilated. Historical final analysis data is available for the period 2000--2014.

The FNL data have a 1° x 1° spatial resolution and are available every six hours.

In this project runs have been made for 4 areas: Indian Ocean, eastern Mediterranean Sea, Bay of Biscay and Baltic. The domain setup for these areas is shown in figures A1 to A6. The target spatial resolution of the WRF domains is 9 km.

In order to make a smooth transition between the 1° x 1° resolution of the FNL data and the target resolution, the WRF model was set up with two nested domains: an outer domain with a 27 km resolution and an inner domain at 9 km resolution.

For each simulation a regular grid is used, defined on a Lambert conformal conical projection. The same grid is used for the CHIMERE runs. However, the outer 5 grid points of the WRF model grid are trimmed before using it.

The model was set up with a model top of 50 hPa and 31 vertical levels. The following physics parameterisations were used:

Table A1 Parameterisations used in the WRF simulations.

Parameterisation type	Name
Microphysics	Ferrier (new Eta) microphysics
Long-wave radiation	RRTM
Short-wave radiation	Dudhia
Surface layer	Monin-Obukhov
Land surface	Unified Noah
Urban	Not used
Boundary layer	YSU
Cumulus	Kain Fritsch (new Eta)

SRTM (Shuttle Radar Topography Mission) data were used to produce the topography for WRF and USGS (United States Geological Survey) data were used to produce the land-use maps.

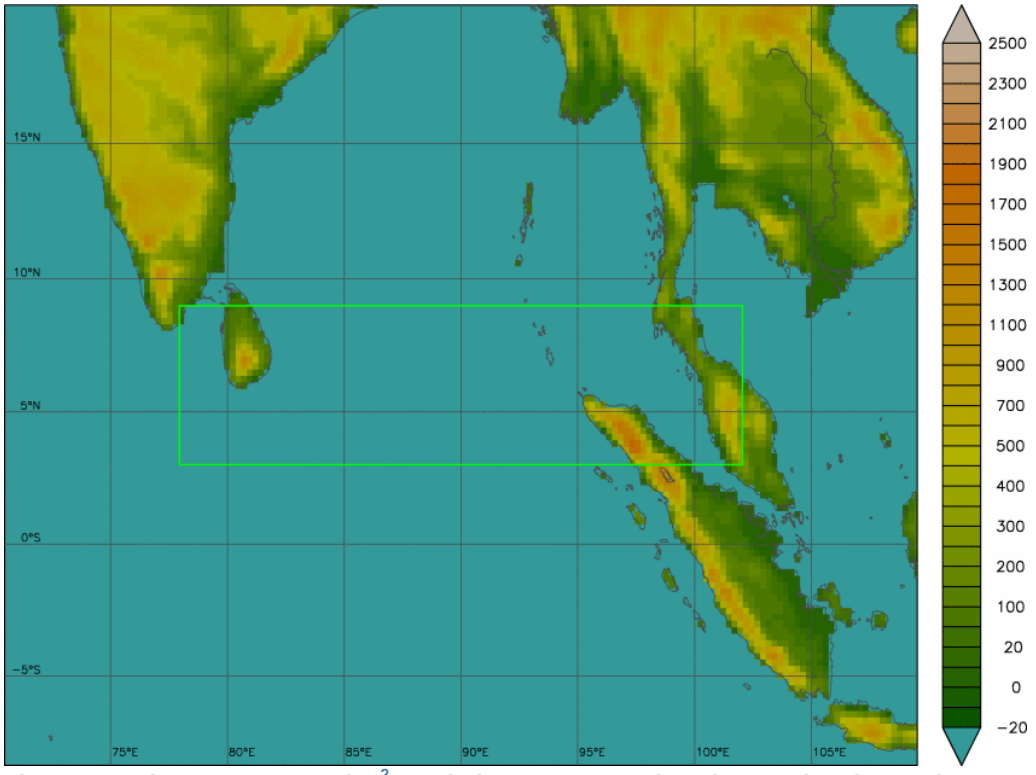

Figure A1 The outer, 27 x 27 km^2 resolution outer WRF domain covering the northern part of the Indian Ocean. The green rectangle marks the location of the 9 x 9 km^2 resolution inner domain. The colour bar indicates surface elevation in m.

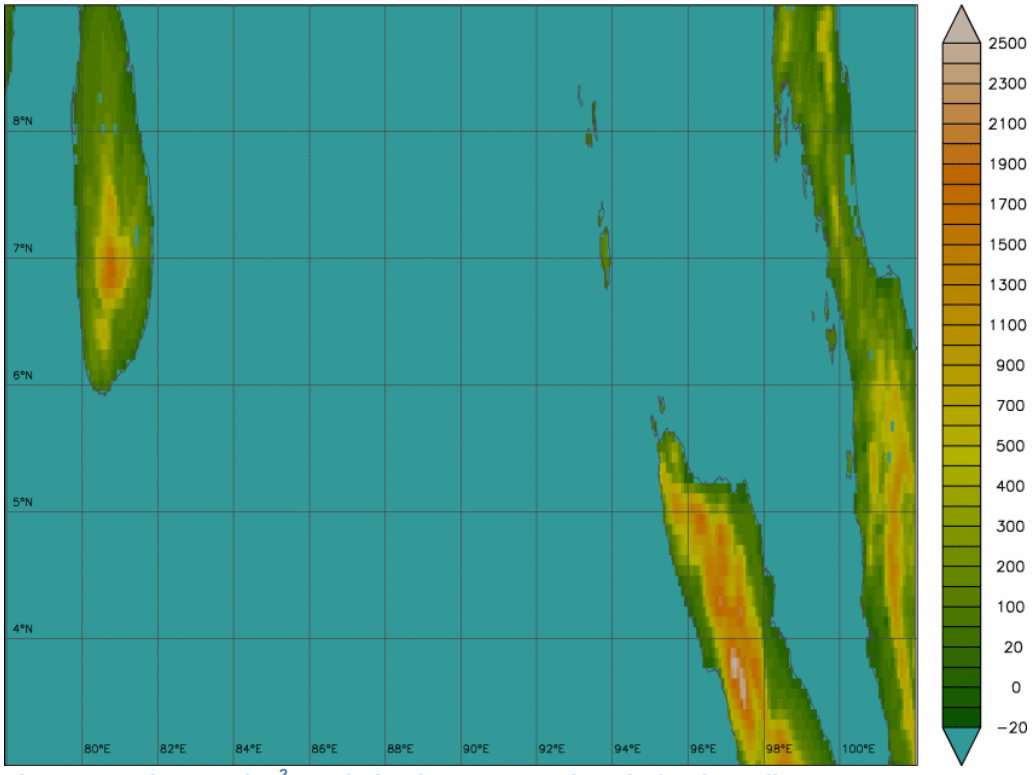

Figure A2 The 9 x 9 km^2 resolution inner, target domain for the Indian Ocean.

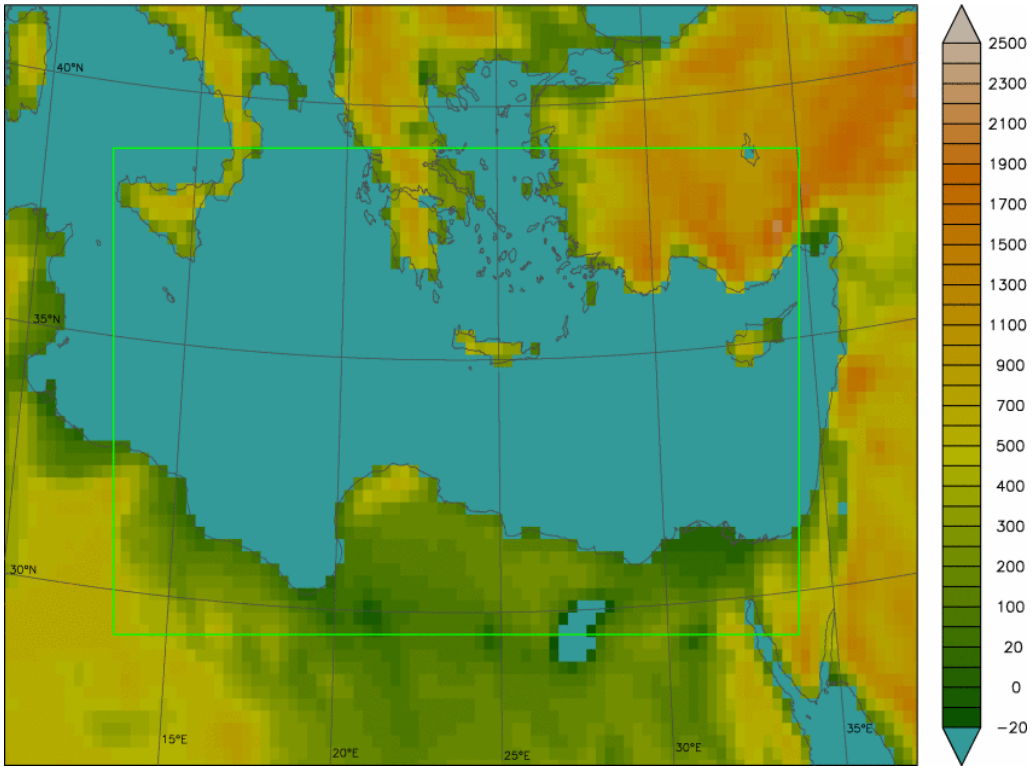

Figure A3 The outer, 27 x 27 km2 resolution outer WRF domain covering the eastern Mediterranean Sea. The green rectangle marks the location of the 9 x 9 km2 resolution inner domain.

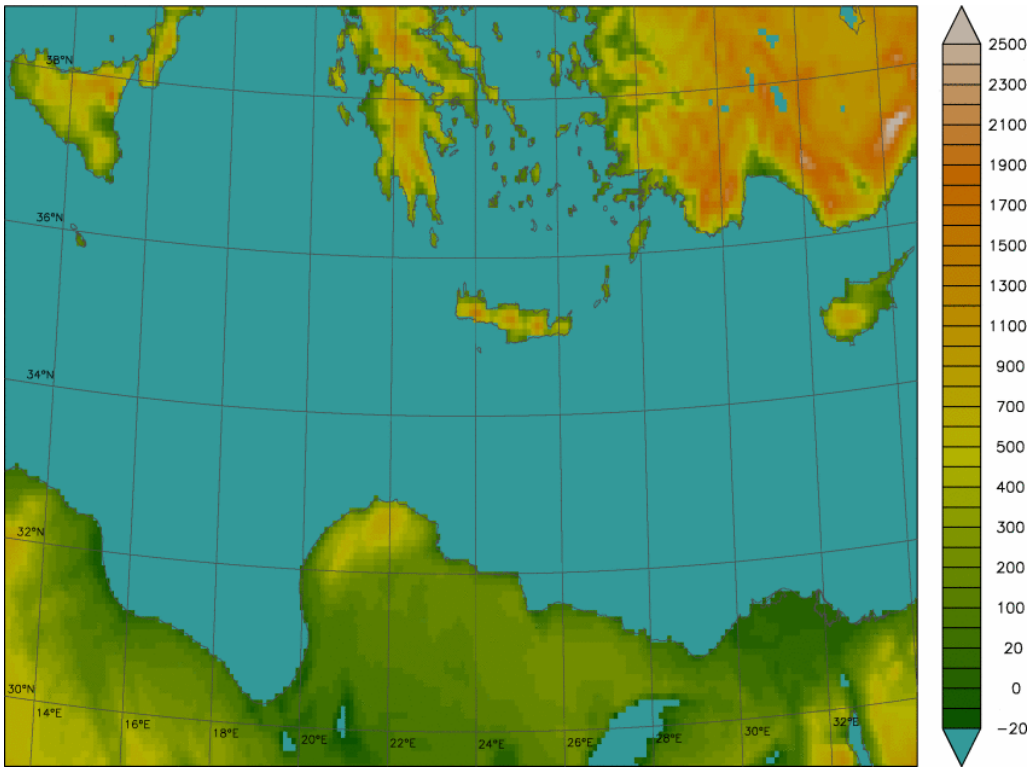

Figure A4 The 9 x 9 km2 resolution inner target domain for the eastern Mediterranean, covering the shipping lane from the Suez Canal to the southern tip of Sicily.

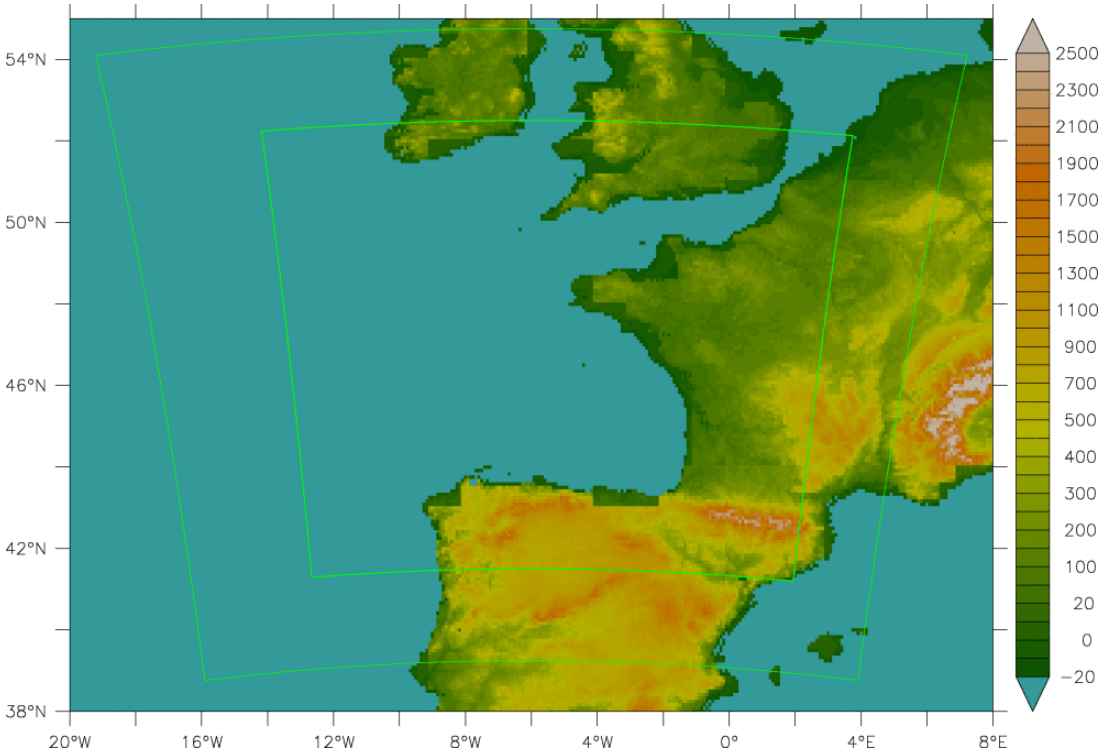

Figure A5 The WRF domain covering the Bay of Biscay. The outer green rectangle marks the 27 x 27 km^2 resolution WRF domain. The inner green rectangle marks the location of the 9 x 9 km^2 resolution domain.

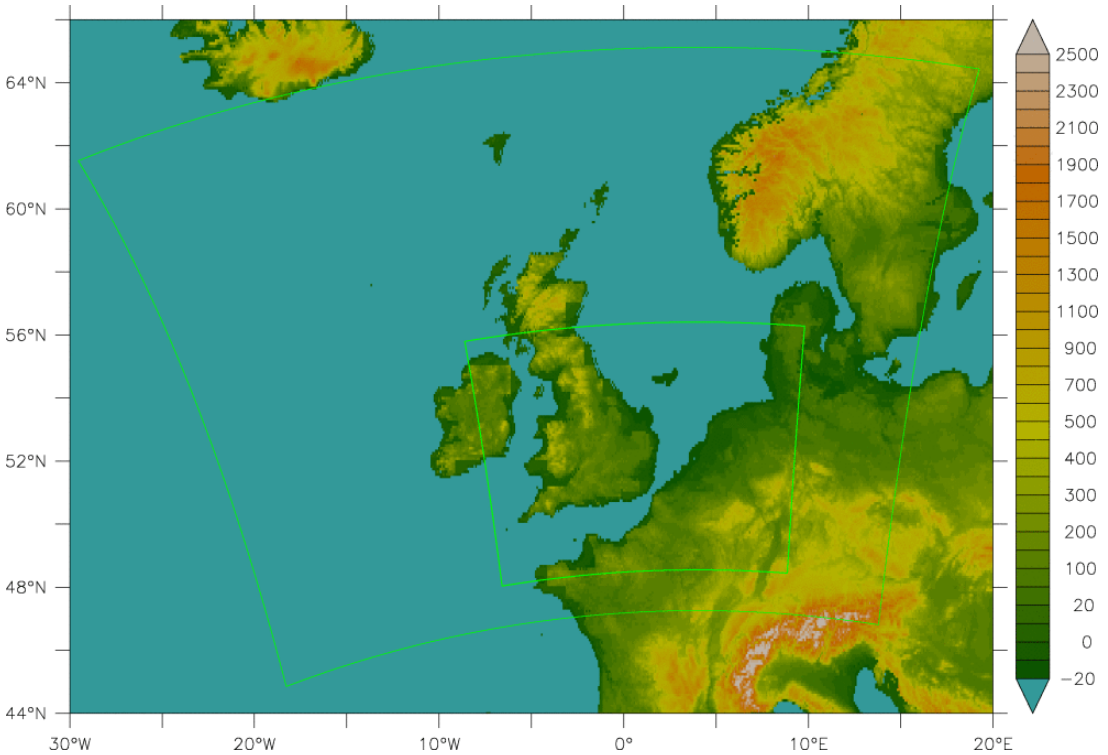

Figure A6 The WRF domain covering the North Sea. The outer green rectangle marks the 27 x 27 km2 resolution WRF domain. The inner green rectangle marks the location of the 9 x 9 km2 resolution domain.

A.1.3 Modelling strategy and output data

The WRF model was run with the domains shown in Figure A1 up to Figure A6 for the year 2007. The model is run for a 48-hour period, and then it is re-initialised using NCEP FNL data. A six-hour long spin-up window is used before the start of each 48-hour period, overlapping with the previous simulation. Spin-up windows are discarded.
The model output consists of data of all major meteorological variables (incl. temperature, wind, pressure, humidity, geopotential height, the height of the planetary boundary layer) on the model grid. The data are available with a temporal resolution of one hour.
The primary weather model variables that are passed on to the chemistry-transport model are

- Temperature (3D)
- Pressure (3D)
- Humidity (3D)
- Wind speed and direction (3D)
- Incoming and outgoing radiation
- Precipitation
- Planetary boundary layer height

A.2 Air quality modelling

A.2.1 CHIMERE chemistry-transport model

The CHIMERE chemistry transport model is developed and maintained under the lead of researchers from the École Politechnique near Paris in France. The model is available under the GNU Public Licence. It can be downloaded from the Internet (see *http://www.lmd.polytechnique.fr/chimere*).

CHIMERE is capable of calculating the changes in air pollutant concentrations due to transport, turbulent diffusion, chemical transformations and deposition. The model requires several input data sets: information on meteorological conditions, boundary conditions (either from climatology or large-scale air quality models), land use data, biogenic emissions, and finally the locations and strengths of anthropogenic emission sources. The meteorological input data are generated in the SEARS project using the WRF model (see previous section).

Like the WRF model, CHIMERE can be applied on a wide variety of spatial scales from local (km or sub-km resolutions) to regional (hundred km resolution). The model can run with several vertical resolutions and with a wide range of complexity. It can use a simplified or a more complete set of chemical mechanisms; it can include or exclude aerosol and organic chemistry. There are also options to include dust uptake by wind, deep convection, urban heat island effects, etc. The temporal resolution of the model is typically one hour.

Table A.2 provides a list of species whose emissions are required by CHIMERE. The model needs the average emissions for each species, per month, per day type (work days, Saturdays and Sundays), and for each hour of the day. The emission data is provided with 6 vertical layers representing pollutants emitted at various altitudes (road surface, chimneys).

Table A.2 Anthropogenic emissions, chemical species required by CHIMERE.

Chimére	Long name
APINEN	Alpha-pinene
BaP	Benzo(a)pyrene
BbF	Benzo(b)fluoranthene
BCAR	Primary black carbon
BkF	Benzo(k)fluoranthene
C_2H_4	Ethene
C_2H_5OH	Ethanol
C_2H_6	Ethane
C_3H_6	Propene
C_5H_8	Isoprene
CH_3CHO	Ocetaldehyde
CH_3COE	Methyl ethyl ketone
CH_3OH	Methanol
CH_4	Methane
CO	Carbon monoxide
H_2SO_4	Sulfuric acid
HCHO	Formaldehyde
HONO	Nitrous acid
NC_4H_{10}	n-Butane
NH_3	Ammonia
NO_2	Nitrogen dioxide
NO	Nitrogen monoxide
OCAR	Organic carbon
OXYL	o-Xylene
PPM_big	Primary PM (d > 10 µm)
PPM_coa	Primary PM (d = 2.5:10 µm)
PPM_fin	Primary PM (d < 2.5 µm)
SO2	Sulfur dioxide
TMB	Trimethylbenzene
TOL	C_7H_8

CHIMERE is primarily designed to produce daily forecasts of ozone, aerosols, and other pollutants and to make long-term simulations (entire seasons or years) for emission control scenarios. The model can be used for the analysis of pollution events, research on various processes, scenario studies and forecasting and warning. Some of the application areas are the analysis of pollution problems in megacities, environmental assessments, health-impact studies, support to (governmental) organisations with their monitoring and reporting duties, short-term air quality forecasts for people with respiratory problems, etc.

A.2.2 CHIMERE pre-processor

The emissions are distributed over the model grid during a pre-processing step. The emission database which is readily available with the CHIMERE model is the EMEP (Co-operative programme for monitoring and evaluation of long-range transmission of air pollutants in Europe) database which has a 50 × 50 km^2 resolution. Emissions of carbonaceous aerosols are available from the LA CAPEDB (Laboratoire d'Áerologie database of emissions for carbonaceous aerosols) with a 0.25° × 0.25° resolution. The EMEP data contain yearly total emissions for a number of emission sectors and pollutants.

It is the task of the CHIMERE emission pre-processor to re-distribute the coarse EMEP emissions to the finer CHIMERE grids using a top-down approach. In broad lines, the pre-processor works as follows:

- Re-distribute the emissions in space based on land-use.
- Re-distribute the emissions in time using country-, sector-, and day-dependent profiles.
- Re-distribute the emissions to altitude levels using sector-dependent vertical profiles.
- Convert the EMEP species to the species needed by CHIMERE using a chemical aggregation/de-aggregation table.

During the land-use based spatial distribution, weights are assigned to the different land-use categories with cities having the largest and forests and water the smallest weight factors.

A.2.3 Emission databases

A chemistry transport model requires input from an emission database. The CHIMERE model was designed to use the EMEP data. However, the emissions in the EMEP database are not available for all project target areas and the 50 x 50 km^2 resolution is too coarse for modelling shipping lanes in the vicinity of land. The EDGAR emission database turned out to be more suitable. For application in this project this database was converted to become EMEP compatible, i.e. format was adapted and activity sectors were remapped.

EMEP emission database

The EMEP emissions database consists of gridded annual national emissions of sulphur oxide (SO_X), nitrogen oxides (NO_X=NO+NO_2), ammonia (NH_3), non-methane volatile organic compounds (NMVOC), carbon monoxide (CO), and particulates ($PM_{2.5}$, PM_{10}). These emissions are provided for 10 anthropogenic source-sectors denoted by so-called SNAP codes.

EDGAR emission database

The following species are available in the global EDGAR database: CH_4, CO, NH_3, NMVOC, NO_x, and SO_2.The data are available in the form of yearly averages, in units of km/m^2/s. The data are gridded and have a resolution of 0.1° x 0.1°. The data are split into IPCC activity sectors (one file per sector and species). The EDGAR v4.2 database was downloaded from: *http://edgar.jrc.ec.europa.eu/overview.php?v=42*.

To bring the EDGAR data in line with the EMEP data, the SO_2 emissions were converted to SO_X using a linear relation and emission values were scaled to change from kg/m^2/s to annual totals.

Redistribution of emissions based on land-use was not applied for the Edgar data, because the resolution is already good enough.

The annual mean NO_X emissions available in the EDGAR database are shown in figure A7. These emissions are pre-processed before entering the CHIMERE processing. The latter result is shown in figure A8. The two results are (almost) identical, confirming that EDGAR data was pre-processed correctly before going into CHIMERE. Figure A8 shows combined results of the 9 km and 27 km domains. Shipping lanes are clearly visible. Range of colour scales for figures A7 and A8 are chosen to enable viewing of shipping emissions. As a result colour scales saturate often for over land areas.

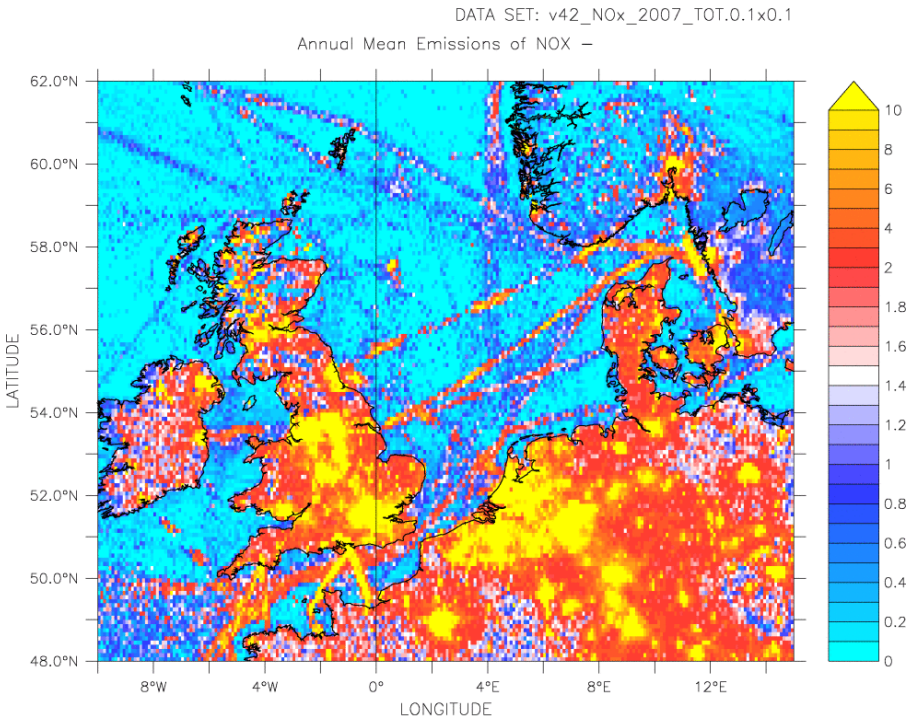

Figure A7 The annual NOX emissions according to the EDGAR database.

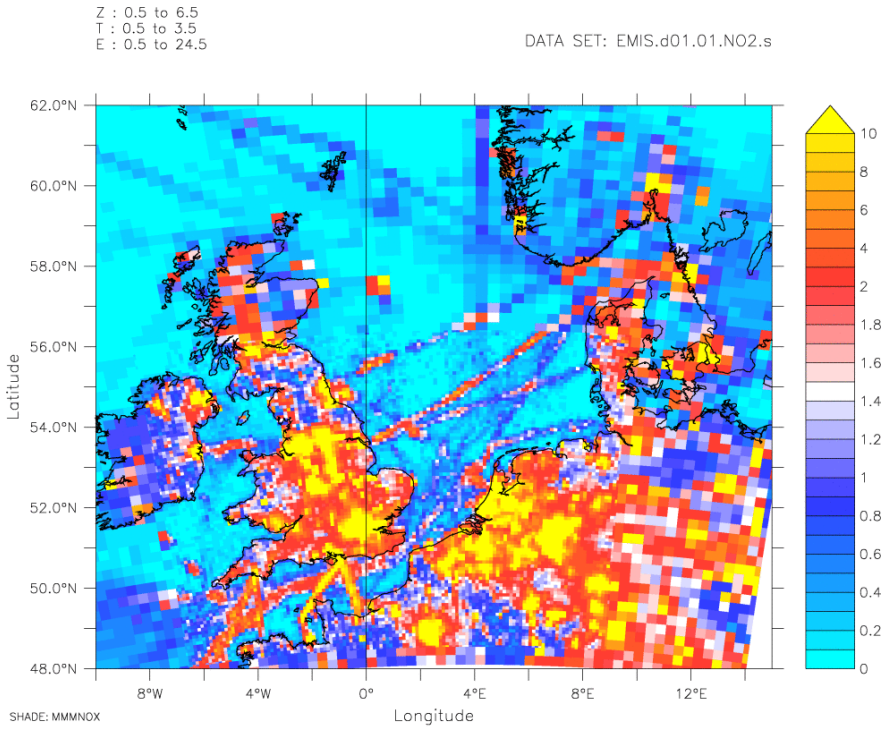

Figure A8 The NOX emissions after passing the CHIMERE pre-processor.

A.2.4 Correspondence between IPCC (EDGAR) and SNAP (EMEP) activity sectors

The EDGAR database uses the IPCC activity sectors which are not the same as the SNAP sectors used by EMEP. The pre-processing of the emissions in CHIMERE and in the BMT ARGOSS emission database is based on the SNAP sectors.

Main EMEP SNAP sectors are:

1. Combustion in energy and transformation industries
2. Non-industrial combustion plants
3. Combustion in manufacturing industry
4. Production processes
5. Extraction and distribution of fossil fuels and geothermal energy
6. Solvent use and other product use
7. Road transport
8. Other mobile sources and machinery
9. Waste treatment and disposal
10. Agriculture and forestry, land use and wood stock change

See also: http://www.emep.int/UniDoc/node7.html

Main EDGAR IPCC sectors are:

1. Energy
2. Industrial Processes
3. Solvents and other product use
4. Agriculture
5. Land use change and forestry
6. Waste
7. Other

See also: http://edgar.jrc.ec.europa.eu/methodology.php#12sou

The corresponding SNAP and IPCC sectors are presented in more detail in table A.3 [ref EMEP report 2013].

Table A.3 Correspondence between SNAP and IPCC activity sectors.

SNAP	SNAP name	IPCC	IPCC name
1	Combustion in energy and transformation industries	1A1	Energy industries
1.1, 1.2	Public power & District heating plants	1A1a	Public electricity and heat production
1.3	Petroleum refining plants	1A1b	Petroleum refining
1.4, 1.5	Solid fuel transformation plants & Coal mining, oil/gas extraction, pipeline compressors	1A1c	Manufacture of solid fuels and other energy industries
3	Combustion and manufacturing industry	1A2	Manufacturing industries and construction
8, 7, 1, 2	Other mobile sources and machinery & Road transport & Combustion and energy transformation industries & Non-industrial combustion plants	1A3	Transport
8.5	Airport and cruise traffic	1A3a	Civil aviation
7	Road transport	1A3b	Road transportation
8.2	Railways	1A3c	Railways
8.4, 8.3	Sea traffic & Inland waterways	1A3d	Navigation
8.10, 1.5	Other mobile sources and machinery & Pipeline compressors	1A3e	Other
2.1-2.3, 8.4, 8.6, 8.7, 8.9	Commercial and institutional plants & Residential plants & Plants in agriculture, forestry and aquaculture & National fishing & Agriculture & Forestry & Household and gardening	1A4	Other sectors
5.1, 4.2	Extraction and first treatment of solid fossil fuels & Coke oven (door leakage and extinction), solid smokeless fuel	1B1	Solid fuels
4.1, 5.2--5.6, 9.2	Processes in petrol industry & Extraction, first treatment and loading of liquid fossil fuels & Extraction, first treatment and loading of gaseous fossil fuels & Liquid fuel distribution (except gasoline) & Gasoline distribution & Gas distribution networks & Flaring in oil refinery and oil and gas extraction	1B2	Oil and natural gas
4.1, 5.2, 5.4, 5.5	Processes in petrol industry & Extraction, first treatment and loading of liquid fossil fuels & Liquid fuel distribution (except gasoline) & Gasoline distribution	1B2a	Oil
5.3, 5.6	Extraction, first treatment and loading of gaseous fossil fuels & Gas distribution networks	1B2b	Natural Gas
9.2	Flaring in oil refinery and oil and gas extraction	1B2c	Venting and flaring
4	Production processes	2	Industrial processes
4.6	Various	2A	Mineral products
4.4, 4.5	Various	2B	Chemical industry
4.6	Various	2D	Other production
4.8	Various	2E	Production of halocarbons and sulphur hexafluoride
6.1 -- 6.5	Various	2F	Consumption of halocarbons and sulphur hexafluoride
6.5.3	Refrigeration and air conditioning equipment using	2G	Other

	other products		
6.1 to 6.5	Various	3	Solvent and other product use
10.4	Various	4A	Enteric fermentation
10.5, 10.9	Various	4B	Manure management
10.1, 10.2	Rice field with/without fertilisers (e)	4C	Rice cultivation
10.1, 10.2, 11.5, 11.6	Cultures with fertilisers & Cultures without fertilisers & N_2O leakage of N into wetlands & N_2O leakage of N into waters	4D	Agricultural soils
	No SNAP sector allocated. Not relevant for Europe	4E	Prescribed burning of savannahs
10.3	Various	4F	Field burning of agricultural wastes
11.21	Various forests, grasslands/tundra and other	5A	Changes in forest and other woody biomass stocks
11.23	Various forests, grasslands/tundra and other	5C	Abandonment of managed lands
10.6, 11.24	Use of pesticides and limestone (CO_2 only) & CO_2 emissions from / or removals into soils	5D	CO_2 emissions and removals from soil
10???	Agriculture and forestry, land use and wood stock change	5F	Biomass burning
9.4	Waste disposal	6A	Solid waste disposal on land
9.10	Waste water treatment and latrines	6B	Waste water handling
9.2, 9.7, 9.9	Various forms of incineration	6C	Waste incineration
5.7	Geothermal energy extraction	7A	Other

A References

EMEP/EEA air pollutant emission inventory guidebook 2013, European Environment Agency report 2013. ISBN 978-92-9213-403-7

Skamarock, W. C., J. B. Klemp, J. Dudhia, D. O. Gill, D. M. Barker, M. G. Duda, X. Huang, W. Wang, and J. G. Powers, 2008: A description of the Advanced Research WRF Version 3. NCAR Tech Notes-475+STR